Atmospheric transport structures shaping the "Godzilla" dust plume

Albert Jarvis [a,*], Ali Hossein Mardi [b], Hosein Foroutan [b], Shane D. Ross [c]

[a] *Department of Mechanical Engineering, Virginia Tech, Blacksburg, VA, USA*
[b] *Department of Civil and Environmental Engineering, Virginia Tech, Blacksburg, VA, USA*
[c] *Department of Ocean and Aerospace Engineering, Virginia Tech, Blacksburg, VA, USA*

HIGHLIGHTS

- Key structures shaping large-scale plumes found via FTLE applied to wind field.
- Northern boundary of Godzilla dust plume is identified as persistent attracting LCS.
- Interactions revealed with jet and vortex which significantly affect plume's fate.
- Comparison between traditional methods and coherent structure methods is performed.

ARTICLE INFO

ABSTRACT

Saharan dust events, having great ecological and environmental impacts, are the largest producers of the world's dust by far. Identifying the mechanisms by which the dust is transported across the Atlantic is crucial for obtaining a complete understanding of these important events. Of these events, the so-called "Godzilla" dust intrusion of June 2020 was the largest and most impactful in the last two decades and underwent a particularly interesting transport pattern. By uncovering dominant, organizing structures derived from the wind velocity fields, known as Lagrangian coherent structures, we demonstrate the ability to describe and qualitatively predict certain aspects related to the evolution of the dust plume as it traverses the atmosphere over the Atlantic. In addition, we identify regions of high hyperbolicity, leading to drastic changes in the shape of the plume and its eventual splitting. While these tools have been quite readily adopted by the oceanographic community, they have still yet to fully take hold in the atmospheric sciences and we aim to highlight some of the advantages over traditional atmospheric transport methods.

1. Introduction

On the third week of June 2020, Aerosol Optical Depth (AOD) measurements of numerous AErosol RObotic NETwork (AERONET) sun photometers located in the Caribbean recorded levels above the long-term background AOD. The observed increase in AOD was caused by a plume of dust, which departed from the western coast of Africa on June 17. The unusual extent and concentration of this African dust plume gave it the "Godzilla" nickname and pushed the 24 h average $PM_{2.5}$ concentration far above the U.S. Environmental Protection Agency's (EPA) 35 μg/m^3 air quality standard in more than 70 air quality measurement stations located in the southeast U.S. on June 26–27 (Yu et al., 2021). The Godzilla dust plume traveled across the Atlantic Ocean, sliding above the marine boundary layer with a maximum plume altitude of 6–8 km and an approximate layer thickness of 3.4 km, showing the characteristics of the Saharan Air Layer (SAL) (Karyampudi et al., 1999; Carlson and Prospero, 1972). Back trajectory analysis

of the receptor regions impacted by this plume denote an average travel speed of 15 m/s, which enabled the plume to travel across the Atlantic Ocean in approximately 8–9 days (Euphrasie-Clotilde et al., 2021). Outside the African continent, the plume maximum density was reached on June 18 with average AOD value reaching as high as 1 and a maximum AOD value above 1.5 (unitless), over an area between 5°N–30°N and 50°W–10°W based on NASA Moderate Resolution Imaging Spectroradiometer (MODIS) data. For the mentioned area, such high amounts of AOD were unprecedented during the month of June since 2002 (Asutosh et al., 2022).

It would be challenging to locate the exact origin of the emissions leading to the Godzilla dust plume but a deep look into the MODIS satellite imagery of days prior to the incident hints at central and western regions of North Africa as the origin of the plume (Remini, 2020). Even though the Godzilla dust intrusion into the Caribbean is categorized as a historic event, dust emissions leading to the formation

of the plume did not show such extreme characteristics. Yu et al. (2021) suggests the modulation of synoptic meteorological conditions as the reason behind the accumulation of dust near the coast of Africa. In their study, the location of a North Atlantic Sub-tropical High (NASH) synoptic system is probed via the NASA Modern-Era Retrospective analysis for Research and Applications, Version 2 (MERRA-2) reanalysis geopotential height at 600 hPa on the days prior to the release of the Godzilla dust plume toward the Caribbean. They note that June 2020 NASH geopotential heights are on average 80 m higher than the 1980–2020 climatology. This study concludes that the specific location of the NASH system, north of the plume and co-occurrence of this geopotential anomaly combined with strong dust emissions from Africa have led to the historic Godzilla dust intrusion. This example of the synoptic condition role in historic dust intrusions further motivates the analysis of air flow over the Atlantic Ocean to determine the inter-connectedness between the flow regime and dust intrusions.

Organizing structures in the atmosphere. Identifying the organizing structures within a geophysical flow is an important part of understanding the transport of a given material under the action of that flow. For example, in the ocean, to know how warm water from the Gulf of Mexico is transported to higher latitudes in the Atlantic ocean, it is important to identify the Gulf Stream and understand its mixing process (Liu et al., 2018). Similarly, in the atmosphere, the spread of wildfire smoke over large distances is determined by atmospheric structures, which may not have a specific nomenclature associated with them (Pretorius et al., 2023; Curbelo and Rypina, 2023). To identify these structures and understand how they evolve, an ensemble air parcel trajectory-based — or so-called Lagrangian — point of view must be taken; this incorporates the time evolution of the flow as the material is transported in it. Streamlines, vector fields, and wind barbs come from velocity data at only an instant in time and often provide little insight for material transport over some finite time window in highly time-dependent flows, like wind velocity fields (Haller, 2015; Günther et al., 2021). In addition, these quantities are frame-dependent and conclusions drawn from them can be skewed based on the frame of reference. As pointed out by Bujack and Middel in a review of flow visualization techniques in the environmental sciences (Bujack and Middel, 2020), these instantaneous (or so-called Eulerian) techniques are commonplace within the atmospheric science community. But they suggest atmospheric flow visualization could benefit from using feature-based extraction techniques and topological methods, like Lagrangian coherent structures.

In fact, transport feature-based methods (LCS and finite-time coherent sets) have been applied to atmospheric applications. The applications have ranged from transport of microbes and aerosols (Tallapragada et al., 2011; Schmale et al., 2012; Peng and Peterson, 2012; Schmale and Ross, 2015; Garaboa-Paz et al., 2015; Nolan et al., 2020a; Pretorius et al., 2023), to hurricane intensification and entrainment (Sapsis and Haller, 2009; du Toit and Marsden, 2010; Rutherford et al., 2012; Ross and Tallapragada, 2012), and the dynamics of the Arctic and Antarctic polar vortices (Joseph and Legras, 2002; Lekien and Ross, 2010; Santitissadeekorn et al., 2010; Serra et al., 2017). However, most of these listed studies were performed by nonlinear dynamicists rather than atmospheric scientists, demonstrating that the atmospheric community has not adopted these methods as readily as the oceanographic community. With this work, we seek to add to the growing body of literature demonstrating the usefulness of these techniques for atmospheric science in the hopes that practitioners will integrate them into their toolboxes. We refer the reader to Günther et al. (2021) for a more detailed comparison of some of the common methods in quantifying atmospheric transport and the benefits of using coherent structure methods.

To study the transport of African dust across the Atlantic Ocean, studies have incorporated a trajectory-based approach to either isolate the source region of dust plumes (Euphrasie-Clotilde et al., 2021;

Alonso-Pérez et al., 2012; Chiapello et al., 1997) or study the transport pattern and geographic region impacted by transported dust (Gläser et al., 2015). To establish a connection between source and receptor regions, either backward trajectories are computed from locations downwind along the prevalent dust transport path or forward trajectories are computed from known source regions during an intense dust emission incident. The robustness of the linkage between the source and receptor regions can be further evaluated using retrievals of dust plumes from satellite remote sensing (Bonasoni et al., 1996; Yu et al., 2013, 2015). In addition, some groups take an Eulerian approach in an attempt to discover the underlying mechanisms of trans-Atlantic dust transport. In this approach, the focus of analysis is on the synoptic conditions from a few days prior to the emission of dust until the dust plume has reached the receptor region. In studies done on the Godzilla storm (Yu et al., 2021; Francis et al., 2020), comparison of anomalies in geopotential height and wind velocity fields relative to the long-term historic climatology (1991–2020) in conjunction with the analysis of the streamlines reveals the underlying atmospheric circulation patterns responsible for emission and transport of dust incidents. In most cases, these patterns point to an anomaly in seasonal weather patterns as possible indicators of historic dust transport incidents. While not a study specific to dust, Chakraborty et al. (2021) identified major aerosol transport pathways across the globe by extending the concept of atmospheric rivers (ARs) for water vapors to aerosol atmospheric rivers (AARs). By doing so, the authors were able to develop a framework to identify extreme aerosol transport events for different major aerosol species and identified AARs specific to dust at the time of the Godzilla storm. Similar to the Lagrangian approach, remote sensing retrievals serve as a real world evaluation for the Eulerian analysis (Pu and Jin, 2021).

Regardless of the approach, identifying possible indicators of anomalous dust incidents can facilitate prediction of them in the future. While these studies are all useful and make major contributions towards the goals they set out to achieve, none tackle the problem of understanding these dust events through the lens of Eulerian and Lagrangian coherent structures. In this paper, we look at the Godzilla dust event and focus mainly on the Lagrangian approach, coupled with some Eulerian diagnostics, with the aim of obtaining a large-scale template for transport while the dust plume was present. By identifying key attracting, repelling, and bounding structures (described below), we obtain a qualitative road map for dust transport during this historic event.

2. Methods

For this work, we mainly focus on methods which we will refer to as "coherent structure methods" which will be described more thoroughly below. We present these tools and their applications in a high-level manner to familiarize the reader with the simplest implementation of these methods. There is a good deal of nuance relating to how certain methods are implemented, differences between some methods, and when it is appropriate to use one over another. We omit most of this discussion from the main text but provide more details for the interested reader in supplemental material.

2.1. Finite time coherent structures

Lagrangian techniques for uncovering patterns related to material transport have become powerful tools over the last few decades (Haller and Yuan, 2000; Shadden et al., 2005; Mancho et al., 2006; Froyland et al., 2007; Dellnitz et al., 2009; Froyland et al., 2010a; Tallapragada et al., 2011; Haller, 2011; Peacock and Haller, 2013; Haller, 2015; Schmale and Ross, 2017; Lopesino et al., 2017; Serra et al., 2020). These techniques were born out of the desire to generalize asymptotic methods from autonomous dynamical systems theory (Strogatz, 2014; Wiggins, 2003) and transfer them to the finite time, nonautonomous

setting, appropriate for realistic geophysical flows. Of these methods, the finite-time Lyapunov exponent (FTLE) and closely related Lagrangian coherent structures (LCS) have emerged as among the most widely used. These methods provide objective (i.e., frame-invariant) diagnostics for extracting the most influential material curves (in a 2D flow) or surfaces (in a 3D flow). The hyperbolic[1] structures derived from the mentioned methods can produce a skeleton for transport in unsteady time-dependent flows, identifying material curves or surfaces responsible for attracting, repelling, and bounding regions of the flow over a time window of interest. To define them, first consider the following initial value problem, viewed as a dynamical system over some general n-dimensional smooth manifold $\mathcal{M}$ (e.g., $\mathbb{R}^3$ or S^2),

$$\frac{d}{dt}\mathbf{x} = \mathbf{v}(\mathbf{x}, t), \qquad \mathbf{x} \in U \subset \mathcal{M}, \quad t \in I \subset \mathbb{R}$$

$$\mathbf{x}(t_0) = \mathbf{x}_0 \tag{1}$$

Then, there exists a family of diffeomorphisms $\{\mathbf{F}_{t_0}^t\}$ (known as the flow maps) associated with the dynamical system given by,

$$\mathbf{F}_{t_0}^t : I \times I \times U \to U$$

$$: \mathbf{x}(t_0; t_0, \mathbf{x}_0) \mapsto \mathbf{x}(t; t_0, \mathbf{x}_0) \tag{2}$$

in which either $t > t_0$ (mapping forward in time) or $t < t_0$ (mapping backwards in time). The flow maps, as depicted in Fig. 1, take points $\mathbf{x}_0$ (or regions A_0) in the fluid at an initial time t_0 and map them to their locations at some other time $t = t_0 + T$ (where T can be positive or negative). To extract features from the flow map, we define the right Cauchy–Green deformation tensor in terms of the linearized flow map (again see Fig. 1),

$$\mathbf{C}_{t_0}^{t_0+T}(\mathbf{x}_0) = (\nabla \mathbf{F}_{t_0}^{t_0+T})^\top \nabla \mathbf{F}_{t_0}^{t_0+T}(\mathbf{x}_0). \tag{3}$$

where ∇ represents the derivative with respect to the initial position $\mathbf{x}_0$ and $T = t - t_0$ is the flow map duration or so-called integration time (which could be positive or negative). The matrix $\mathbf{C}_{t_0}^{t_0+T}(\mathbf{x}_0)$ is symmetric and positive-definite with real eigenvalues λ_i and corresponding orthonormal eigenvectors ξ_i with $i \in \{1, 2, \ldots, n\}$ such that,

$$\lambda_1 \geq \cdots \geq \lambda_n > 0 \text{ and,} \tag{4}$$

$$\langle \xi_i, \xi_j \rangle = \delta_{ij}. \tag{5}$$

There is a variational theory for hyperbolic LCS (Haller, 2011) wherein the structures are found by identifying solution curves of the maximum and minimum eigenvector fields of $\mathbf{C}_{t_0}^{t_0+T}(\mathbf{x}_0)$ which satisfy certain conditions relating to their influence on material deformation relative to nearby solution curves. The variational LCS method provides a way to find the precise surfaces which dominate fluid-parcel deformation over the interval T of interest, but such surfaces are often quite costly to compute, can be challenging to implement, and have recently been shown to lack robustness to uncertainty in velocity data relative to other coherent structure methods (Badza et al., 2023). Alternatively, the FTLE (a finite-time analogue of the classic Lyapunov exponent) field is a scalar field that is related to the average exponential rate of stretch of initially (infinitesimally) nearby particles over the time window of interest. Note that the maximum eigenvector of $\mathbf{C}_{t_0}^{t_0+T}(\mathbf{x})$ gives the direction in which an infinitesimal perturbation will undergo the maximum growth (given by $\sqrt{\lambda_1}$ or equivalently $e^{\sigma|T|}$) over the finite time window $[t_0, t_0 + T]$ where σ is the FTLE, defined as,

$$\sigma_{t_0}^{t_0+T}(\mathbf{x}_0) = \frac{1}{2|T|} \log(\lambda_1) \tag{6}$$

While the FTLE field still requires a significant amount of particle integration, the numerical implementation can be optimized via parallel computing, significantly reducing the computation time. We use an in-house python package, that makes use of parallelization and just-in-time compilation, that allows for quick computation even with very large data sets, and in spherical coordinates appropriate for global geophysical flows.

Often, ridges of the FTLE field can be used as a proxy for hyperbolic LCS (Shadden et al., 2005) and the easiest way to identify ridges is to simply use a thresholding method which only looks at FTLE values above a certain threshold, yielding regions of high stretching in forward or backward time. Other methods exist to extract curves (in 2D) that usually coincide with hyperbolic LCS. Care should be taken when implementing these methods and one should be aware of potential pitfalls as they can sometimes result in false positives in regions of high shear if additional criteria is not satisfied along the ridge (Haller, 2011) (see S1 of the Supplementary Materials for more details). Later on, we link to a video of LCS overlaid on FTLE which confirms that all of the important structures we focus on are indeed attracting LCS.

For this work, we start by focusing on backward time FTLE fields, yielding attracting coherent structures (see Fig. 2). The main reason we do this is to elucidate the predictive capabilities of these methods and demonstrate their usefulness for real-time decision making. These structures are computed over the time window $[t_0 - T, t_0]$ where t_0 is the current time. Attracting structures are computed using only current and past velocity data and therefore can be implemented in (essentially) real-time to inform decision making in time-sensitive applications, since the velocity data is readily available. By contrast, repelling structures (think the inverse behavior of Fig. 2) are computed over the time window $[t_0, t_0 + T]$ and therefore require future velocity data for their computation. This necessitates forecasting of the velocity fields to make use of them for real-time decision making, introducing further error and uncertainty.

While attracting structures are computed from the backward time system, due to the continuity of the flow and their dominance relative to nearby material lines, they tend to persist for at least *some* portion of the future time window, preserving their usefulness in the predictive setting, as will be demonstrated. In addition, in recent work (Pretorius et al., 2023), attracting structures have been shown to act as "air bridges" (see Fig. 2, left) in large-scale ($\sim 1,000$ km) atmospheric flows, behaving as pathways for material to be transported along. We were interested to see if these air bridges persisted on much larger scales (a few thousand kilometers). What we found suggests that the "air bridge" concept may still be relevant, but its role in transport depends on which side of the bridge the material of interest began on (see Fig. 2).

2.2. Instantaneous coherent structures

In addition to computing the structures mentioned above which require a certain duration T, one can compute *instantaneous* structures, requiring the velocity only at a single instant t_0. These instantaneous structures are the finite-time coherent structures as the finite-time T goes infinitesimally to zero and like their finite time counterparts, they are also objective, providing an attractive alternative to other common Eulerian quantities. Using only the current data frame, they are simple to compute and often can illuminate important short time structures/regions within the flow. These structures arise out of the eigenvalues and eigenvectors of the Eulerian rate-of-strain tensor, given by:

$$\mathbf{S}(\mathbf{x}_0, t) = \frac{1}{2} \left(\nabla \mathbf{v}(\mathbf{x}_0, t) + (\nabla \mathbf{v}(\mathbf{x}_0, t))^\top \right) \tag{7}$$

where $\mathbf{S}(\mathbf{x_0}, \mathbf{t})$ is a symmetric matrix with real eigenvalues s_i and corresponding orthonormal eigenvectors $\mathbf{e}_i$ with $i \in \{1, 2, \ldots, n\}$ such that,

$$s_1 \geq \cdots \geq s_n \text{ and,} \tag{8}$$

$$\langle \mathbf{e}_i, \mathbf{e}_j \rangle = \delta_{ij}. \tag{9}$$

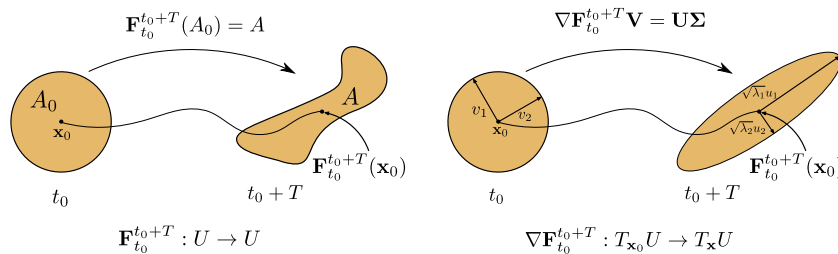[1] 'Hyperbolic' means that the structures exponentially attract or repel nearby material.

Fig. 1. Left: Action of the flow map on a point $\mathbf{x}_0$ and enclosing set A_0 over the time window $[t_0, t_0 + T]$. $\mathbf{F}_{t_0}^{t_0+T}$ acts on elements of the domain and maps them to the domain. Its action on a set can be defined in the following manner: $\mathbf{F}_{t_0}^{t_0+T}(A_0) := \{\mathbf{F}_{t_0}^{t_0+T}(\mathbf{x}_0) \in U | \mathbf{x}_0 \in A_0\}$. Right: Action of the linear approximation of the flow map acting on an infinitesimal circle defined by vectors v_1, v_2 over the time window $[t_0, t_0 + T]$. The derivative of the flow map, $\nabla \mathbf{F}_{t_0}^{t_0+T}$, acts on elements of the tangent space (i.e., vectors) based at $\mathbf{x}_0$ and maps them to elements of the tangent space downstream at $\mathbf{x} = \mathbf{F}_{t_0}^{t_0+T}(\mathbf{x}_0)$. The meaning of the eigenvalues and eigenvectors of $\mathbf{C}_{t_0}^{t_0+T}$ can equivalently be seen through the SVD of $\nabla \mathbf{F}_{t_0}^{t_0+T} = \mathbf{U}\mathbf{\Sigma}\mathbf{V}^*$. The singular values ($\text{diag}(\mathbf{U})$) are equal to the square root of the eigenvalues ($\sqrt{\lambda_i}$) and the right singular vectors (v_i) are equal to the eigenvectors (ξ_i).
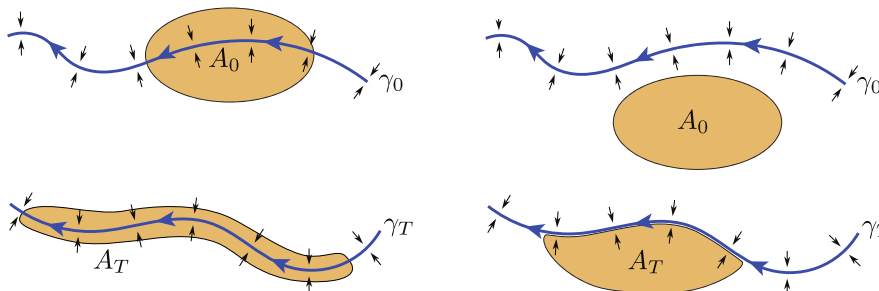

Fig. 2. Behavior of initial blob A_0 straddling an attracting LCS (left) which acts as an "air bridge" and an initial A_0 below the same attracting LCS (right) after some finite time window of interest.

Following Nolan et al. (2020b), in a $n = 2$ dimensional flow, denote s_1 (respectively, s_2) by s_+ (resp., s_-), which are instantaneous Lyapunov exponents (iLEs). The iLE field is the limit of the FTLE field as integration time goes to 0,

$$\lim_{T \to 0^{\pm}} \sigma_{t_0}^{t_0+T}(\mathbf{x}_0) = \pm s_{\pm}(\mathbf{x}_0, t_0) \tag{10}$$

where the superscript $\pm$ on 0 denotes whether the limit is from above ($+$) or below ($-$). In this work, we compute the iLE field to identify a region of the plume which undergoes significant instantaneous hyperbolic deformation.

2.3. Vortex identification

Throughout our analysis, we identify vortex structures in the FTLE field that play an important role in the evolution of the dust plume. Identifying vortices by way of FTLE is not standard and we make an attempt to use more common methods to confirm the structures we are focusing on are indeed vortices. In addition, while we make no claims that the storms we find are cyclones (or anticyclones), we show that they exhibit some common characteristics of cyclones, further demonstrating the strength of these storms. We look at a few basic diagnostics for identifying storms. Mean sea level pressure (MSLP) maps are looked at during the formation of these vortices to see if low pressure systems can be identified. Low level (850 hPa) vorticity is also probed to find highs in these fields, a common characteristic of strong storms and cyclones. Cyclone identification involves considerably more complexity than just these diagnostic methods, and there are many different schemes to detect these storms (Camargo and Zebiak, 2002; Bauer et al., 2016; Chang, 2017; Walker et al., 2020), but we are not concerned with whether or not the structures we identify are properly defined cyclones. Our main focus is on how other structures in the FTLE field interact with these storms. To this end, we simply aim to confirm that these storms behave like vortices. With this in mind, the final diagnostic we look at is the Lagrangian averaged vorticity deviation (LAVD), an objective quantity used to find rotationally coherent

vortices in a flow, known as elliptic LCS (Haller et al., 2016). Assuming we have a system (1) with corresponding flow map (2), the vorticity at any point $\mathbf{x}$ will be given by $\boldsymbol{\omega}(\mathbf{x}, t) = \nabla \times \mathbf{v}(\mathbf{x}, t)$. Then, the instantaneous spatial mean of vorticity is given by:

$$\bar{\boldsymbol{\omega}}(t) = \frac{\int_U \boldsymbol{\omega}(\mathbf{x}, t) dV}{\text{vol}(U)}, \tag{11}$$

where $\text{vol}(\cdot)$ represents the volume (3d) or area (2d) and dV represents either a volume or area element. From there, the LAVD is defined as

$$\text{LAVD}_{t_0}^t(\mathbf{x}_0) := \frac{1}{|t - t_0|} \int_{t_0}^t |\boldsymbol{\omega}(\mathbf{x}(s, \mathbf{x}_0), s) - \bar{\boldsymbol{\omega}}(s)| ds, \tag{12}$$

which can be computed either forward or backward in time but, it has been noted that the different time direction calculations will generally result in different elliptic LCS (Haller, 2023). To identify the boundaries of these coherent vortices, the outermost closed, convex contour surrounding a local maxima is extracted to serve as the elliptic LCS. In this work, we are less interested in extracting the curves themselves and use the LAVD field as a diagnostic for identifying coherent vortices.

2.4. Data and software

NASA MERRA-2 data (see Fig. 3) is used to create the wind velocity fields with a $0.5° \times 0.625°$ horizontal resolution, 42 pressure levels of vertical resolution, and a 3-hourly temporal resolution. MERRA-2 is a continuation of the former NASA MERRA reanalysis dataset with an improved meteorology and atmospheric model, generated by the NASA Global Modeling and Assimilation Office (Gelaro et al., 2017; Bosilovich et al., 2015). MERRA-2 wind data (Global Modeling and Assimilation Office (GMAO), 2015) is chosen due to nominal coverage and widespread application and validation in the literature (Carvalho, 2019; Khatibi and Krauter, 2021). MSLP and low level vorticity are obtained from the ERA5 dataset (Hersbach et al., 2023b,a), which is the European Centre for Medium-Range Weather Forecasts (ECMWF) fifth-generation reanalysis dataset for the global climate and weather of the past eight decades. Datasets are available hourly in a gridded
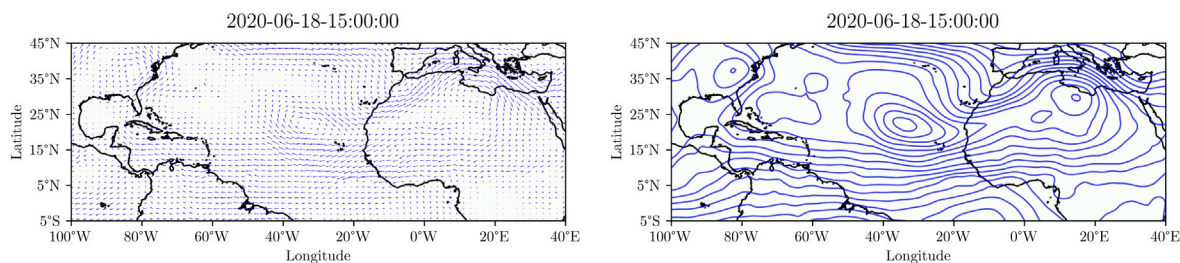
Fig. 3. From MERRA-2 for 2020-06-18-15:00:00. Left: Velocity field in region of interest. Right: Corresponding streamfunction.

format with a spatial resolution of $0.25° \times 0.25°$ and vertical coverage of 1000 hPa to 1 hPa on 37 vertical pressure levels. For streamfunction and vorticity calculations from MERRA-2 data shown later, the wind-spharm python package (Dawson, 2016) is used which utilizes spherical harmonics to compute these quantities. All other diagnostics (FTLE, iLE, and LAVD) and feature extraction (LCS) are performed by an in-house software package available on GitHub.

To isolate the dust plume, the ultraviolet Aerosol Index (AI) values from the Ozone Mapping and Profiling Suite (OMPS), installed on the Suomi-NPP satellite are used, which is the official AI product provided by NASA (Torres, 2019) (see Fig. 4). Suomi-NPP has a sun-synchronous orbit, meaning that it passes the equator at the same local mean solar time on each pass with multiple swathes covering Earth's surface on each day. Hence, to create daily dust plume images, multiple swathes covering a region between 5°S–45°N and 100°W–35°E on each day are selected and averaged to a pixel size of 0.5°. The OMPS AI product is a unitless columnar value representing the atmospheric aerosol concentration from Earth's surface up to the sensor height, with higher AI values representing higher aerosol concentrations. Both dust and smoke aerosols are UV absorbing and therefore contribute to the AI values (Yang et al., 2013) but considering our latitudes of interest and extent of the dust plume, we believe the impact from other types of aerosols are negligible. As we seek a comparison with 2D vertical column-averaged aerosol index data, we use column-averaged vector fields (Nolan et al., 2020a) where the averaged velocity fields come from pressure surfaces ranging from 500 hPa–800 hPa. These pressure surfaces are where the dust was mostly present, as estimated from a previous study (Pu and Jin, 2021).

2.5. Caveats with implementation

The approach mentioned above results in a 2D time-varying column averaged quasi-velocity field. This vector field is no longer a *true* velocity field as it does not describe the velocity of a true fluid parcel anymore. Care should be taken when employing an approach like this. The resulting vector field need not be incompressible anymore and it is perhaps possible, depending on the velocity fields being averaged, to obtain structures in the FTLE field which are artifacts of the averaging. In our case, we show that the field is indeed incompressible and the main structures we focus on are not artifacts of the averaging by comparing with FTLE obtained from a common pressure surface used in the literature for this event (600 hPa). For more details on why we chose this approach and potential problems this could cause if due diligence is not performed, we refer the reader to section S2 of the Supplementary Material.

The dust concentration we focus on evolves due to the both advective and diffusive processes. FTLE and standard LCS were developed solely in the context of advective transport. More recently, theory has been developed which takes diffusion into account in the weakly diffusive case (Haller et al., 2018). Out of this work comes the diffusive barrier strength (or sensitivity) field (DBS), which acts as a diffusive counterpart to FTLE. Although utilizing DBS could potentially offer greater accuracy and relevance, this paper focuses on presenting the simplest and most commonly recognized technique among Lagrangian

coherent structure methods: FTLE. It is important to clarify that DBS is not inherently complex; it merely involves additional steps beyond FTLE, along with some increases in memory overhead and computational cost. However, considering our goal to engage practitioners effectively, we suggest that readers might prefer using existing FTLE codebases. There are numerous FTLE implementations available, compared to the relatively limited number for DBS. This availability could be a decisive factor in the choice of methods for practical application. Furthermore, it has been noted in Haller et al. (2018) that, unless the diffusion structure tensor is sufficiently anisotropic or the underlying velocity field has significant temporal aperiodicity, the DBS field will not differ significantly from the FTLE field. To be sure we are not missing anything substantial, we compare the FTLE to the DBS over a large domain used in a later section (see video).

In addition to the diffusive considerations, dust particles are inertial (not neutrally buoyant) and their density differs from that of air. For this reason, a more accurate representation of the structures could be obtained by computing inertial FTLE (iFTLE) or inertial LCS which uses the Maxey–Riley equations in the particle integration step of the FTLE computation to capture the inertial effects of the particles (Sudharsan et al., 2015; Tallapragada and Ross, 2008). Along with the additional computational expense, doing this would require estimating the Stokes number and size of the dust particles. However, we show that using the simplified[2] method captures dominant structures related to transport and evolution of the dust plume.

3. Results

Using data retrieved from MERRA-2, we begin by computing backward FTLE for an integration time of 96 h (4 days) from June 5, 2020 to June 30, 2020. The integration time chosen should generally be tied to some characteristic time scale of the flow or the material being transported by the flow. If too short a time is chosen, there is a risk of missing important structures, and if too long of a time, often one ends up with an overly complicated set of LCSs from which it is hard to derive meaning. The plume takes ~8 days to traverse the Atlantic Ocean. We tested a variety of integration times ranging from 1 day to 8 days. We settled on 4 days since this was roughly half the time it took for the dust to traverse the Atlantic and produced satisfactory FTLE fields. See S3 of the Supplemental Material for more details. Here, we demonstrate a simplified implementation of the coherent structure methods for the problem at hand to highlight the robustness of these methods.

We focus on the affected area where latitude runs from 5°S–45°N and longitude runs from 100°W–35°E but use the global velocity field in

---

[2] We note that we are in the density regime in which particles will more strongly be attracted to passive attracting ridges (dust is an "aerosol" or a heavier particle than the carrier fluid and the Stokes number is not small) as opposed to the case when the inertial particles are lighter than the carrier fluid (known as "bubbles"), in which case passive attractors act more like repellers and the inertial particles aggregate away from these structures. See the mentioned references for more details. In the regime we are in, the simplification becomes more justified.
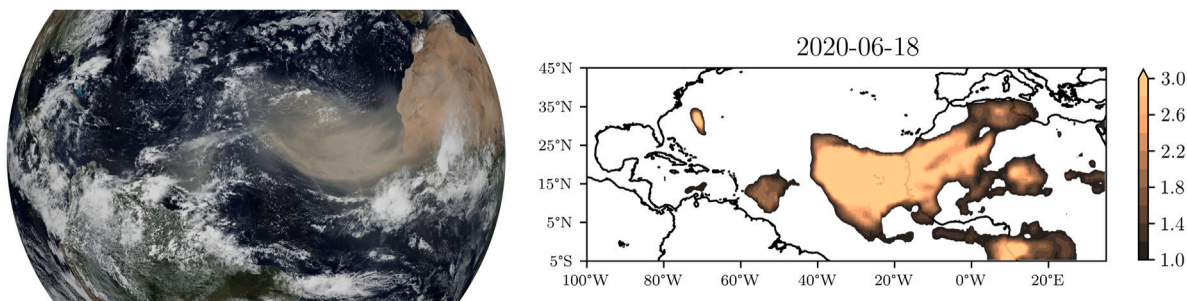
Fig. 4. Left: Godzilla dust plume, June 18, 2020 (Credit: NASA). Right: Aerosol Index data (unitless) from OMPS (see video). These values are used throughout the paper.
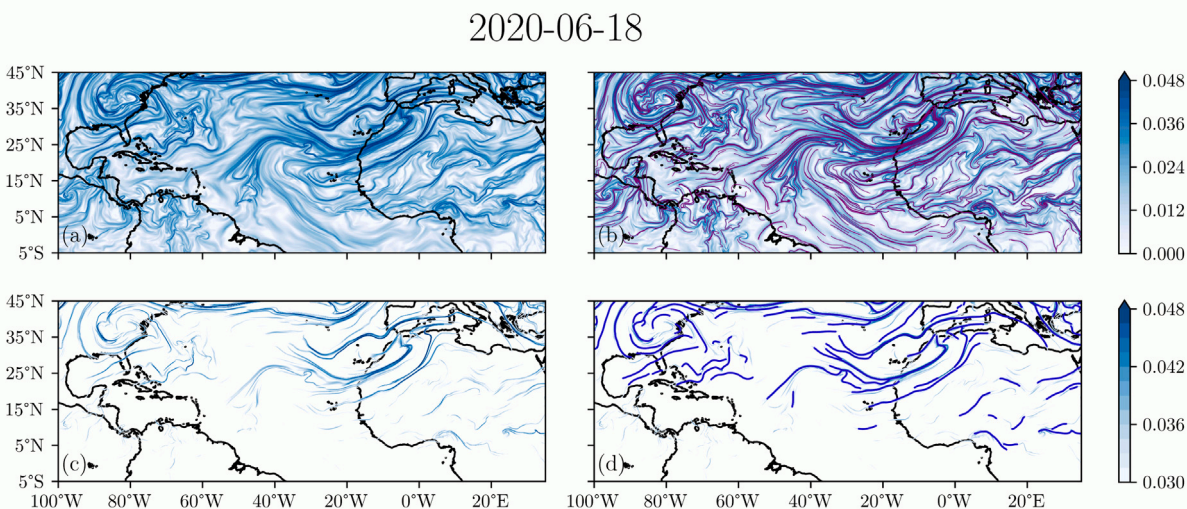

Fig. 5. (a): Backward FTLE field (hr^{-1}) at same time as composite image via satellite (see FTLE video). (b): Attracting LCS (purple) found via variational method overlaid on backward FTLE field. (c): Simple thresholding method used to obtain dominant regions. (d): Ridge detection algorithm used to obtain ridges of interest. These values in the colorbar are used for the remainder of the paper.

our FTLE calculations (see Fig. 5). The aerosol index data provided by OMPS representing the actual extent of the dust plume was overlaid on the region of interest. For the coherent structures we present, a simple thresholding method is used for both the fields of interest (to obtain ridges corresponding to dominant attracting/repelling structures) and the aerosol index data (in an attempt to focus on the dust plume itself) with the aim of demonstrating the effectiveness of a comparatively simple-to-use and computationally inexpensive approach for real-time decision making. If one is interested in obtaining actual curves instead of visible ridges of a scalar field, which is useful when quantities normal and tangent to the ridge are desired, a ridge detection algorithm can be deployed (Shadden et al., 2005; Senatore and Ross, 2011; Steger, 1998) to obtain these structures from the FTLE field. Alternatively, LCS be found with the variational method. We show both approaches in Fig. 5. Note that the relatively high threshold value we have adopted may result in the omission of numerous LCS, but these are of lower strength (as the FTLE, and thus ridge height inherently measures). These omitted structures are generally of lesser importance for the analysis of large-scale transport phenomena that we aim to investigate. This thresholding approach was deliberately chosen to prioritize the identification and analysis of the most influential and large-scale structures, aligning with our research objectives. If one was interested in obtaining more of the LCS, ridge detection could be performed without any thresholding.

The results are organized as follows: we discuss the backward FTLE field overlaid with OMPS aerosol index data in the region of interest, making note of significant features, some of which we will analyze in greater detail in later sections. This subsection represents

what could be done with FTLE in essentially real-time with enough computing power (only current and past data is used) and access to relatively accurate velocity data. Following this, we include the forward FTLE field to see what is gained by incorporating forecast wind data.[3] Then, we make comparisons with Eulerian quantities by highlighting areas where they provide insight and demonstrate that the FTLE field helps us understand, and in some cases predict, phenomena which the Eulerian quantities simply cannot. In subsequent figures we will highlight certain features we are describing with arrows or boxes if we feel they are not obvious from their description alone. In S4 of the Supplemental Material, we produce the same figures that will be covered in sections 3.1 and parts of 3.2 but using velocity fields from the 600 hPa pressure to make sure we are not missing any important structures or observing any artifacts due to the averaging.

3.1. FTLE

On June 1, 2020, a vortex starts to form to the north-northwest of the plume, off the northwest coast of Africa. We refer to this as the early June vortex in later sections. We omit the figures showing its formation as this is less important. A video of the backward FTLE ridges overlaid on OMPS aerosol index data can be seen here. In addition, we provide a video of attracting LCS, computed using the variational

---

[3] Here we still use MERRA-2 reanalysis data so this would be assuming the forecast data is as accurate as reanalysis data. Results would be effected if true forecast data was used.
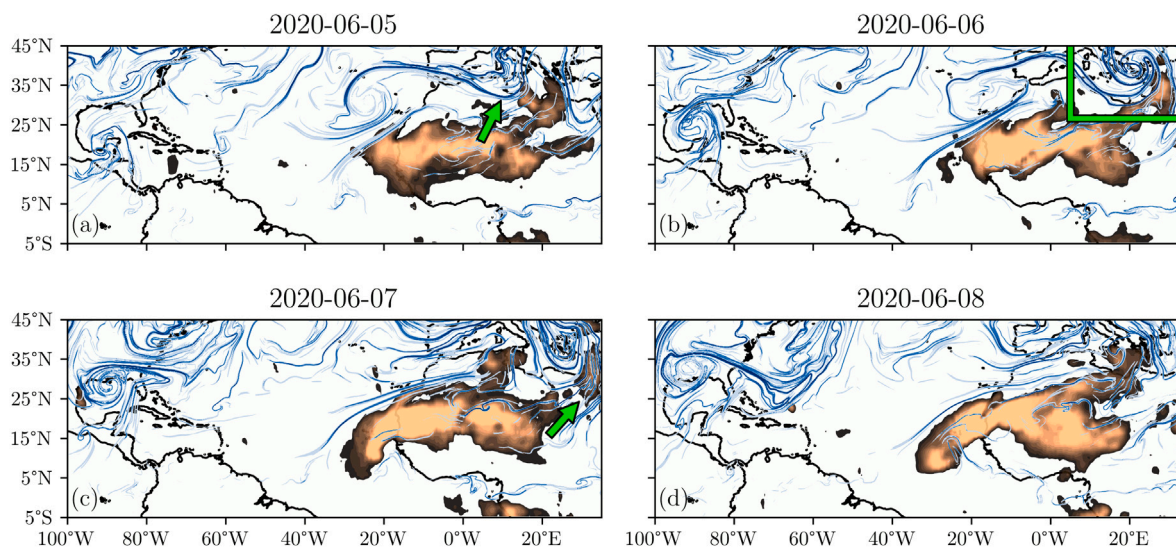
Fig. 6. Backward FTLE ridges overlaid on aerosol index data obtained from OMPS, June 5–8, 2020. See text for details.
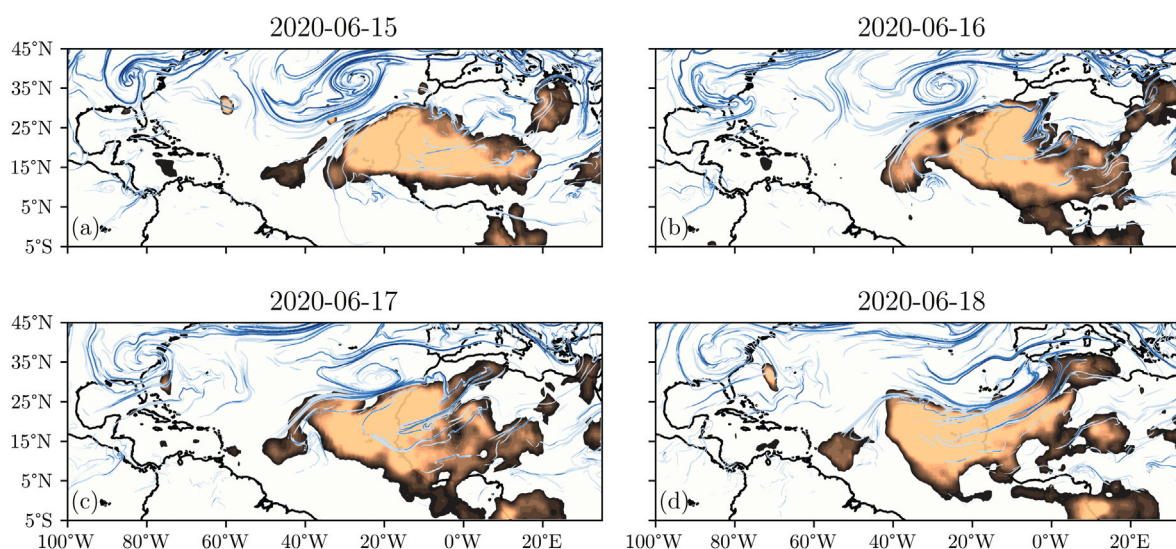

Fig. 7. Backward FTLE ridges overlaid on aerosol index data obtained from OMPS, June 15–18, 2020.

method, overlaid on the backward FTLE field to confirm the structures we are focused on are true hyperbolic structures and not FTLE false positives due to shear. The vortex hovers in this area until about June 5 (Fig. 6a), when a FTLE ridge forming the northern piece of this vortex (green arrow in 6a)) forms another vortex (green box Fig. 6b) and they are both shepherded to the east while the original early June vortex dissipates and has little effect on the plume. As this happens, the secondary vortex breaks off a piece of the plume over northern Africa and pushes it towards southeast Asia (green arrow in Fig. 6c). These type of vortex structures, made up of regions of high deformation, will be important in describing the evolution of the plume. In addition, there is a strong attracting ridge acting as the northern boundary for the plume. This ridge persists throughout a large portion of the plume's lifetime and prevents transport to the north.

For the next two days, the plume does not change in shape much and hovers over northwest Africa, moving north slightly as it is attracted to the strong ridge acting as its northerly boundary. On June 12, a new vortex begins to form in roughly the same place as the early June vortex (off the coast of northwest Africa). We will refer to this vortex as the mid June vortex and first show it on June 15 (Fig. 7a). At first, this vortex seems quite similar to the early June

vortex and one might expect a similar minor effect on the plume. But this time, as the northern attracting ridge is attracted towards the vortex, the vortex is propelled towards the plume and collides with it directly. As it does, the vortex dissipates and spreads out but its effect on the plume is substantial. The vortex pushes down on the plume and drastically deforms its northern boundary, flattening and elongating it as it propels the western portion further west at a more rapid rate than it was originally traveling. We see the results of this collision in Fig. 8. A mushrooming effect is taking place on June 19 (Fig. 8a) as the western portion grows and begins to separate from the rest of the plume. This becomes more pronounced on June 20 (Fig. 8b) and then a split happens on June 21 (Fig. 8c); all the while a strong attracting ridge bounds the main plume to the north, its shape changed by the earlier collision. By June 23 (Fig. 9a), the plume has fully split into separate pieces. As this happens a strong ridge runs between the two. Starting on June 24 (Fig. 9b) a new feature becomes evident. We see a ridge running through the middle of the plume, acting in a similar manner to the air bridges seen in other transoceanic smoke transport (Pretorius et al., 2023). Furthermore, a "FTLE front" becomes apparent (Fig. 9c,d) that ushers the new mushrooming portion of the plume westward towards the Americas.
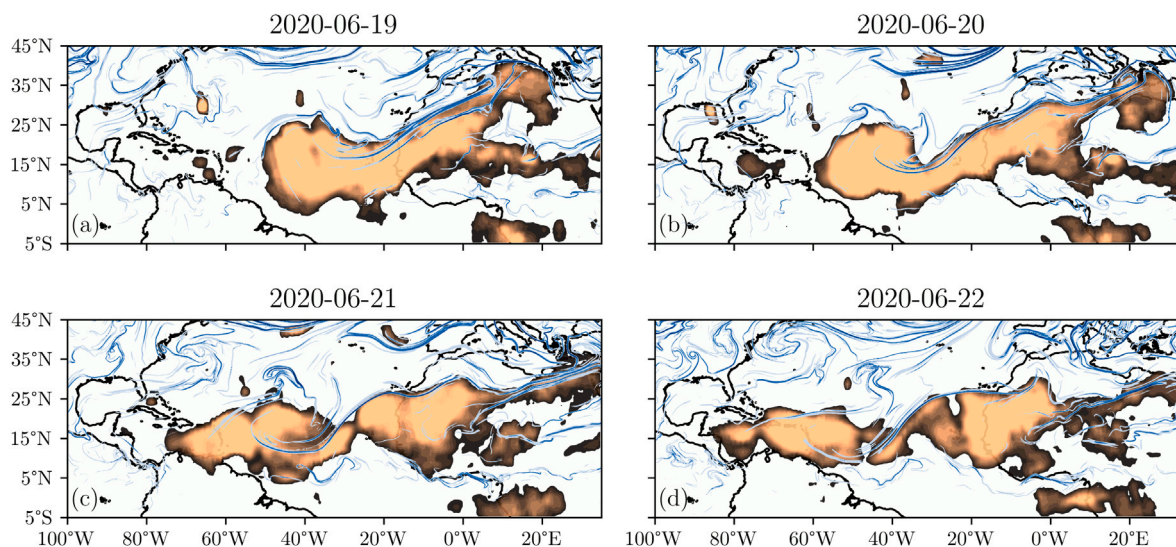
Fig. 8. Backward FTLE ridges overlaid on aerosol index data obtained from OMPS, June 19–22, 2020.
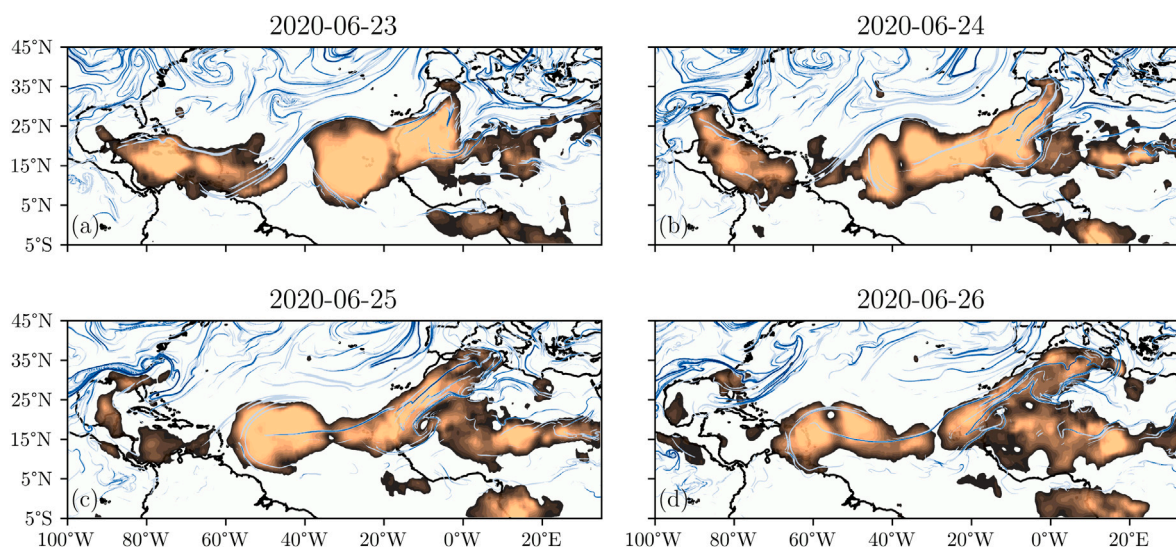

Fig. 9. Backward FTLE ridges overlaid on aerosol index data obtained from OMPS, June 23–26, 2020.

In Figs. 10–12, both backward *and* forward FTLE ridges are overlaid with dust data (see video) to see what is gained from incorporating future (originally, forecast) data. On June 11 (Fig. 10a) we notice some repelling ridges near the southwestern portion of the plume. On June 12 (Fig. 10b), these ridges connect and, on the 13th (Fig. 10c), we notice there are some repelling ridges intertwined with the strong mid June vortex structure mentioned previously. This behavior is usually indicative of cyclonic storm behavior (e.g., hurricanes) but storms in this region are not classified by NOAA so there is no mention of it in the literature. In addition, we can see the repelling ridge near the southern portion of the plume being drawn to and eventually connecting with the repelling ridges in the vortex. This connection creates "turnstile lobes" (MacKay et al., 1984; Meiss, 1992; Coulliette and Wiggins, 2001; Shadden et al., 2006) that could be useful for identifying sets of particles that will remain separate from the vortex and those which will be entrained into it; see Sapsis and Haller (2009), du Toit and Marsden (2010), Rutherford et al. (2012), Ross and Tallapragada (2012). For example, had this storm been over the plume and one had information about the locations of dust associated microbes present, predictions could be made about which of these would be ejected from the plume and subsequently entrained into the vortex as it traversed the Atlantic (Tallapragada et al., 2011; Schmale and Ross, 2015).

On June 15 (Fig. 11a), repelling ridges can be seen in between the vortex structure and the northern attracting ridge. On June 16 (Fig. 11b), we can see one of these repelling ridges essentially being sandwiched between the two dominant attracting structures and being ejected towards the east at a rapid rate. This is behavior that is indicative of strong stretching (in dynamical systems terms, hyperbolic) events and we see this play out in subsequent days as the plume stretches and undergoes strong hyperbolic deformation, especially at the northern portion. We see similar behavior on June 18 (Fig. 11d) with a few ridges intersecting the northerly attracting ridge and being pulled to the east, producing further hyperbolic deformation. Finally, during June 19–21 (first shown as green arrow in Fig. 12a), there is a repelling ridge intersecting the main attracting ridge. It is hard to say for sure with the temporal resolution for the dust data limited to 24 h averages, but it seems this intersection point may lead to more hyperbolic behavior and assist in the eventual splitting of the plume.

3.2. Eulerian combined with Lagrangian analysis

In this subsection, we focus on some of the phenomena mentioned above and observe where Eulerian information is useful and where it
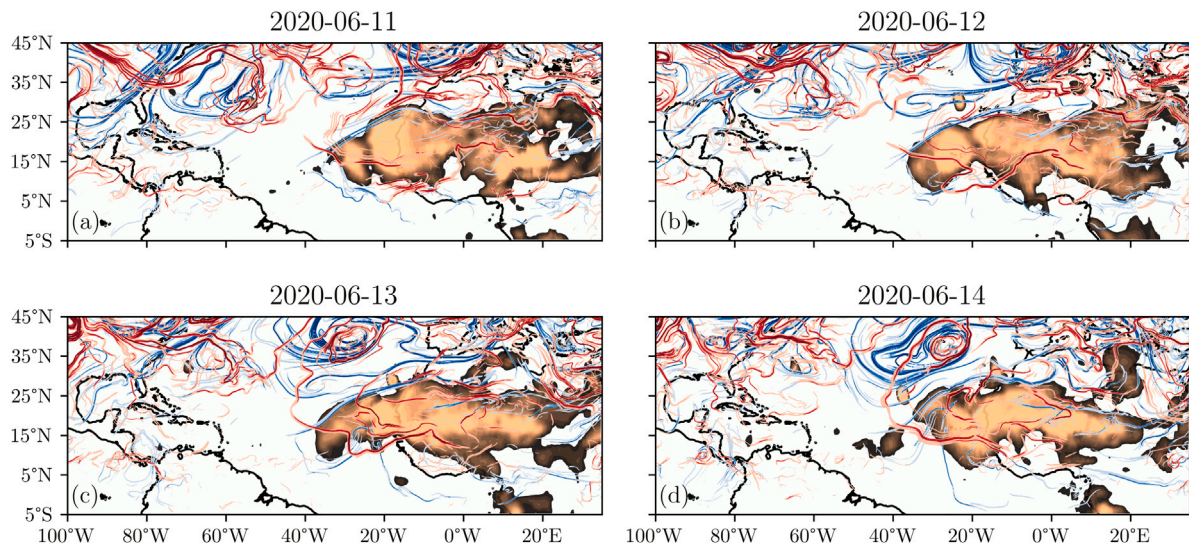
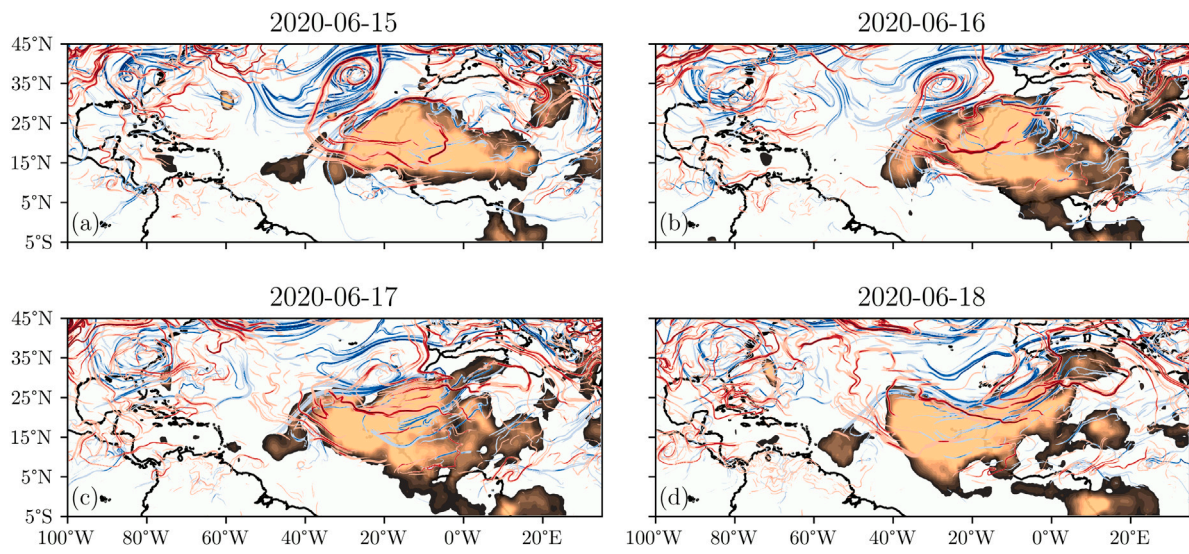**Fig. 10.** Forward and Backward FTLE ridges overlaid on aerosol index data obtained from OMPS, June 11–14, 2020.

Fig. 11. Forward and Backward FTLE ridges overlaid on aerosol index data obtained from OMPS, June 15–18, 2020.
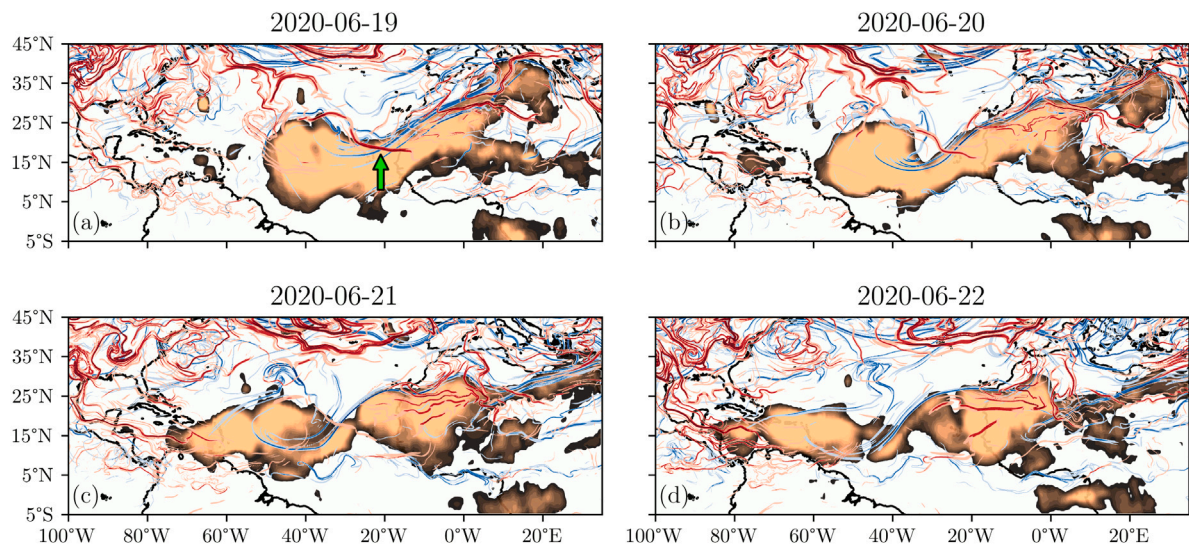

Fig. 12. Forward and Backward FTLE ridges overlaid on aerosol index data obtained from OMPS, June 19–22, 2020. See text for details.
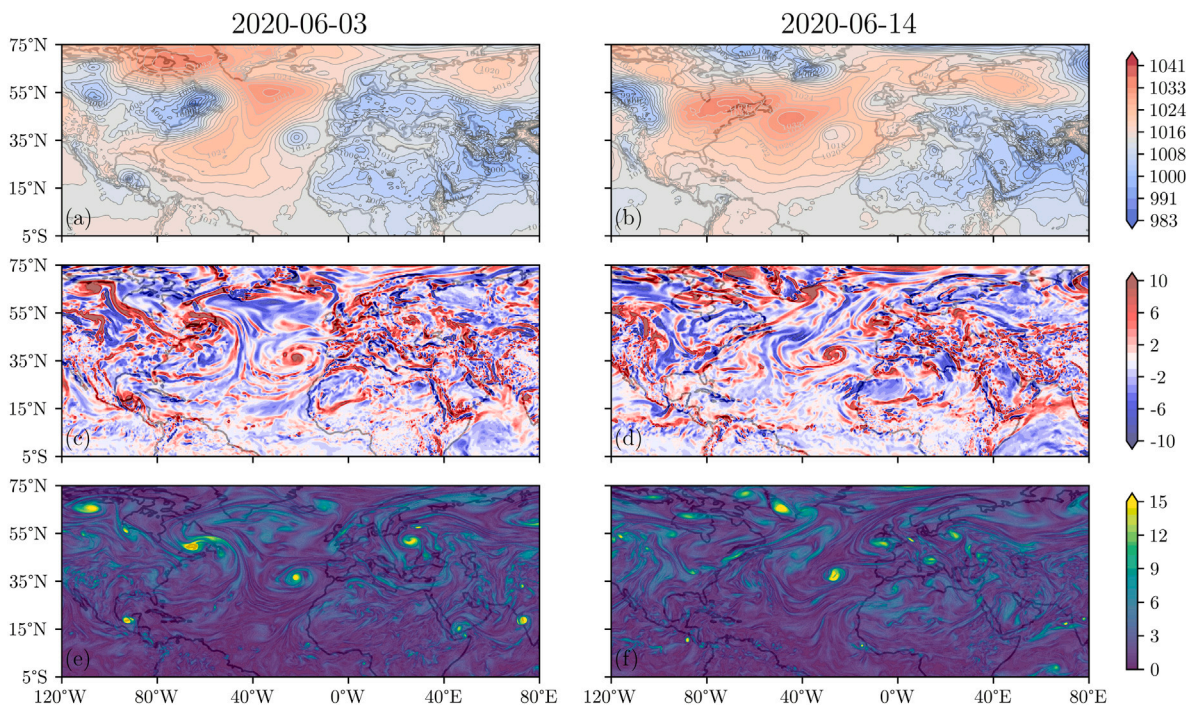
Fig. 13. MSLP (hPa, top), low level vorticity at 850 hPa ($10^{-5} \times s^{-1}$, middle), and LAVD ($10^{-5} \times s^{-1}$, bottom) on June 3, 2020 (left) and June 14, 2020 (right).

falls short when compared to the Lagrangian diagnostics mentioned above. There are three main phenomena to discuss. First, we will compare the early June and mid June vortices and attempt to uncover why two seemingly similar structures had drastically different effects on the fate of the plume. Then, we will see if the strong northern ridge, which bounded the plume for most of its lifetime, could have been identified using Eulerian information. Finally, we will focus on the splitting of the plume in late June and again see if any Eulerian quantities could have indicated that this would happen.

Early June and mid June vortex comparison. In the following figures, we take a wider view and focus on the area where latitude runs from 5°S–75°N and longitude runs from 120°W–80°E to better see the effects of other FTLE features on the plume. We begin by identifying the vortices by looking at the mean sea level pressure (MSLP), low level vorticity (at 850 hPa), and backward Lagrangian averaged vorticity deviation (LAVD), which is computed for an integration time of 1 day using the averaged velocity fields. For these figures, the focus is on the region with center around 25°W, 35°N, off the northwest coast of Africa. On June 3, we notice a low in the MSLP (Fig. 13a). On June 14, the MSLP (Fig. 13b) in the region of the vortex is not quite as low, but is a low relative to the surrounding high. For the low level vorticity, we notice highs for both June 3 (Fig. 13c) and June 14 (Fig. 13a). In addition, we see local maxima in the LAVD field on both dates (Fig. 13e,f), indicating a coherent vortex in the center of the storm that has persisted from at least one day ago. These figures seem to indicate that the early June vortex is the stronger of the two with a lower low and more coherent/strong center as seen in the vorticity and LAVD fields. Much of the same is drawn from the following day. Again the early June vortex shows as a low in the MSLP (Fig. 14a) and the mid June vortex shows as a relative low while surrounded by a strong high (Fig. 14b). Highs are again seen in both low level vorticity fields (Fig. 14c,d) and local maxima can be seen in the LAVD fields (Fig. 14e,f). The mid June vortex seems to be strengthening as can be seen by its more coherent vortex center. Through these figures we can confirm that we are indeed looking at true vortex structures. In addition, these storms can be seen in the satellite imagery as apparent on the NASA page for this dust event. Now, we move on to focusing on other features in the FTLE field which interact with these structures.

In the subsequent figures, the early and mid June vortex patterns are in different columns (early June left, mid June right), while we show the velocity field and FTLE field in the rows (velocity top, FTLE bottom). A full video of the comparison of these two fields was also produced. The reader is encouraged to watch the comparison video as much of what is described in this section is much easier seen in the video. In addition, we again provide a video of attracting LCS overlaid on the backward FTLE field to confirm the structures we are focused on are truly hyperbolic. Looking at the velocity fields (Fig. 15a,b), a counter-rotating vortex pattern is apparent (Newton, 2001), both in the early and mid June vortices identified earlier, but also in a larger vortex over northern Africa that kept the plume in place before the collision with the mid June vortex. Interestingly, one might argue the early June vortex is the "stronger" of the two and therefore would be the one having a greater effect on the plume. Observations could be made about the velocity field above the vortex structures, over Europe, and to the northwest, over North America. In early June there is a strong vortex to the north while this does not exist in mid June. In early June there are more vortex patterns to the northwest and more of a jet feature in mid June. In both of these cases it is hard to say with any confidence how these patterns will effect the early and mid June vortices. Conversely, the FTLE ridges yield influential material lines that will be advected with the flow and affect nearby particles as they come in contact. In early June, the ridge making up the northern portion of the vortex is long and is connected to other regions of the flow running north through eastern Europe (green box in Fig. 15c) while the mid June vortex is less "connected" as its northern ridge remains separate from the strong ridge off the western coast of Europe and the one running through eastern Europe (green arrow Fig. 15d). While not of immediate interest, we note the FTLE activity over North America. There is quite a bit more going on in mid June compared to early June which can be most easily seen in the video, where a jet feature is present in the FTLE field.

In Fig. 16, we begin to fully see the distinction between the effects of the early and mid June vortices on the fate of the plume. There is a similar story in the velocity fields; one notices differences between the early and mid June features. In early June (Fig. 16a) it is difficult to see why the vortex was simply pulled towards the east in comparison to the
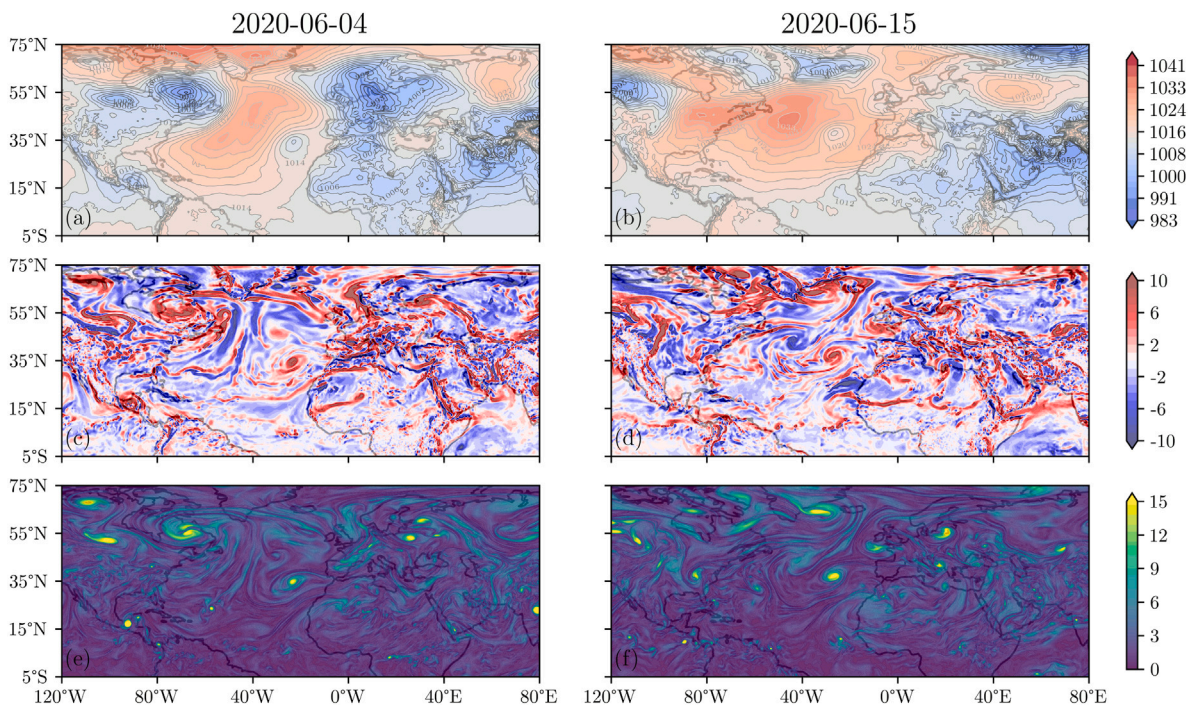
Fig. 14. MSLP (hPa, top), low level vorticity at 850 hPa ($10^{-5} \times s^{-1}$, middle), and LAVD ($10^{-5} \times s^{-1}$, bottom) on June 4, 2020 (left) and June 15, 2020 (right).
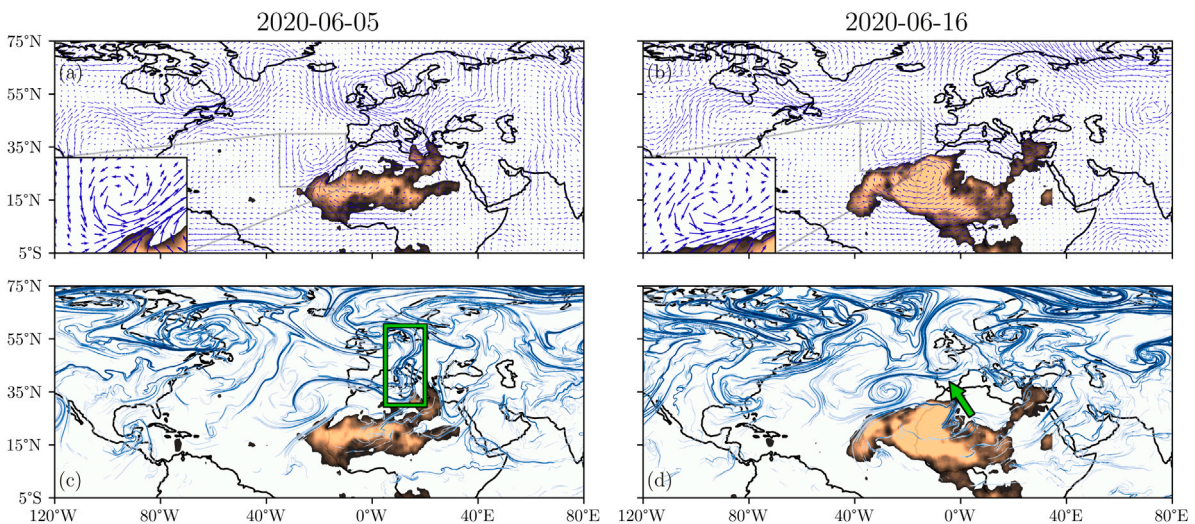

Fig. 15. Velocity field (top) and backward FTLE ridges (bottom) overlaid on OMPS aerosol index data on June 5, 2020 (left) and June 16, 2020 (right). See text for details.

trajectory of the mid June one (Fig. 16b). There is a jet feature present in mid June to the northwest that is somewhat apparent in the Eulerian data but one cannot conclude from this data alone that it would have as great of an effect on the mid June vortex as it did. When we look at the FTLE fields, things become more clear. In early June, the vortex is being pulled along by the secondary vortex mentioned earlier, to which it is connected. In addition, it is being influenced and swept along by a large FTLE pattern over Europe (green box in Fig. 16c). In mid June, the jet feature is now more apparent (magenta box in Fig. 16d) with a small vortex being created at the end of the jet. This leads to a mushrooming effect with a FTLE ridge leading the way (green box in Fig. 16d), which pushes on the vortex and propels it into the plume. In the final figure (Fig. 17) we see the effects of these interactions and the drastic difference in the shape of the plume after the early and mid June vortices run their courses. The key difference here is that the velocity field shows the direction and instantaneous speed of a fixed point in

space, allowing one to loosely infer where/how particles in the flow are actually moving while the FTLE field actually shows us how material in the flow is moving (by identifying the most influential material lines and *seeing* them move through space), allowing for much more detail and insight to be extracted when focusing on transport events.

Dust plume northern boundary. There are other Eulerian quantities which can be used to compare to FTLE or help better analyze this transport event. We go through them briefly here, providing only a frame for each but with an accompanying video if the reader is interested. Consider the video performing the same comparison as was done between FTLE and velocity fields, but with the corresponding *streamfunction* instead. Many of the same conclusions are drawn as with the previous comparison. Note that the streamfunction does not identify the northern boundary (see Fig. 18 and video mentioned previously).

On the other hand, the *vorticity* field provides significant insight, capturing the strong northerly boundary FTLE ridge as a curve of
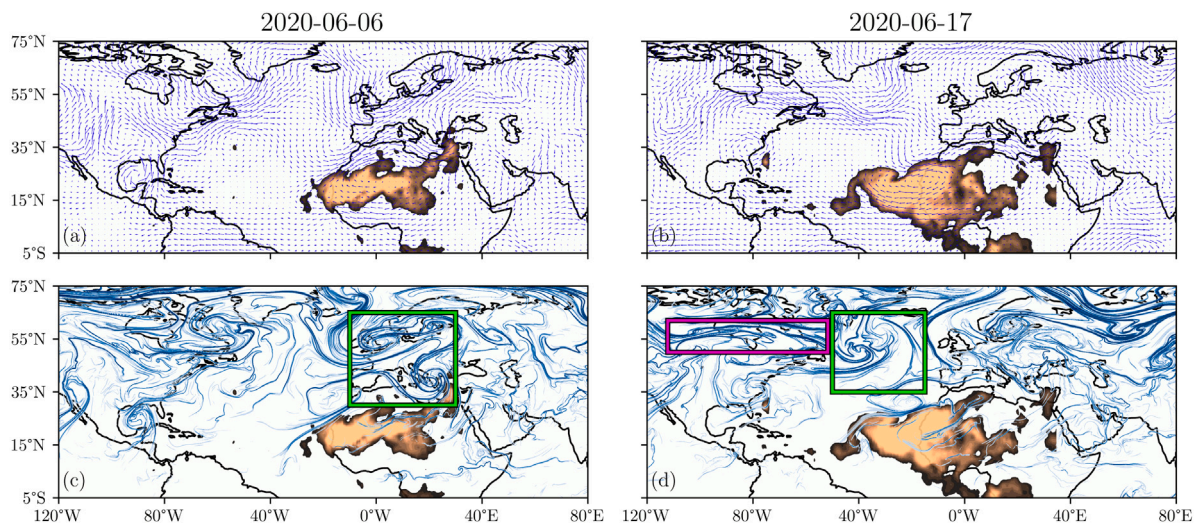
Fig. 16. Velocity field (top) and backward FTLE ridges (bottom) overlaid on OMPS aerosol index data on June 6, 2020 (left) and June 17, 2020 (right). See text for details.
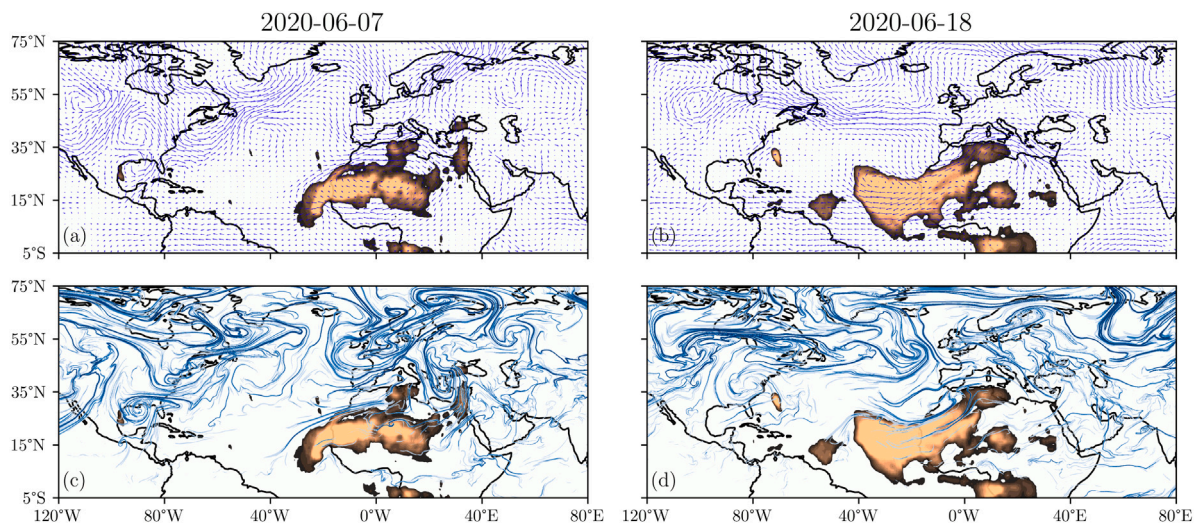

Fig. 17. Velocity field (top) and backward FTLE ridges (bottom) overlaid on OMPS aerosol index data on June 7, 2020 (left) and June 18, 2020 (right).
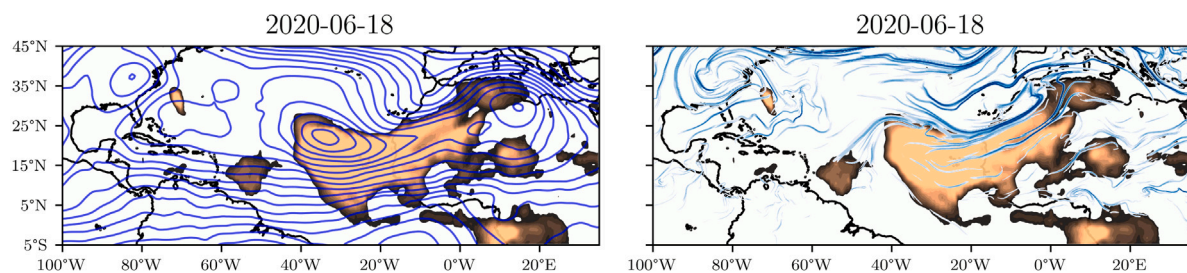

Fig. 18. Left: Streamfunction overlaid on OMPS aerosol index data. Right: Backward FTLE overlaid on aerosol index data.

vanishing vorticity; see Fig. 19 (left) and the full video. Note that there are many other zero vorticity contours not associated with FTLE ridges. The FTLE ridge as the northern plume boundary instills confidence that it will indeed be a significant transport barrier, as it is objective (independent of the frame of reference) whereas vorticity is not objective and the FTLE takes into account information from the entire past time window.

Finally, we turn to an objective Eulerian diagnostic, the instantaneous Lyapunov exponent (iLE) field mentioned earlier. The iLE field quantifies instantaneous deformation and gives credence to the large

effect of the mid June vortex collision with the plume. As seen in Fig. 19 (right), as the mid June vortex collides with the plume we see very large iLE values along the plume's northern portion. Recall the iLE is the limit of the FTLE field as the integration time goes to zero, providing an objective diagnostic for identifying regions of high attraction and repulsion at an instant in time. The high values along the northern portion confirm that the plume underwent large scale deformation at the time of impact with the vortex. A full video of the iLE field overlaid on the dust data and backward FTLE ridges is provided here.
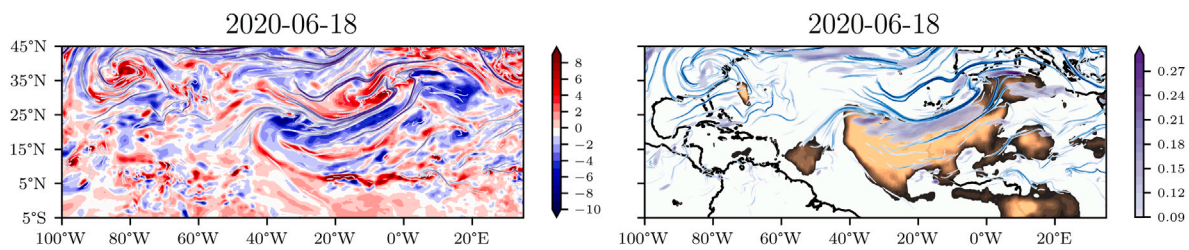
Fig. 19. Left: Backward FTLE ridges (purple) overlaid on vorticity ($10^{-5} \times s^{-1}$, blue and red). Right: iLE ($10^{-6} \times s^{-1}$, purple) field overlaid on backward FTLE ridges (blue) and OMPS aerosol index data (copper) on June 18, 2020.

Plume splitting event. We end our analysis by looking at the splitting event of the plume around June 21. Recalling Fig. 12a, we see an intersection point (green arrow) between the forward and backward FTLE ridges near where the splitting takes place. Forward and backward FTLE ridges can essentially be considered as time-dependent analogues of stable and unstable manifolds (Shadden et al., 2005; Sadlo and Weiskopf, 2010; Bujack et al., 2019) and therefore, their intersections can be thought of as time-dependent analogues of saddle points.[4] These points can be important as they sometimes behave as moving, transient saddle points, having a similar effect, locally, on the flow nearby. Clearly they can be identified by looking for intersections between the forward and backward FTLE ridges (attracting and repelling LCS intersections are sometimes referred to as "generalized saddles") but we were curious if we could find these points, or regions near these points, by using only current and past data. We focus on the specific point we refer to at the beginning of this section as we believe it played a role in the splitting of the plume. We did not find any Eulerian data on its own that identified this point or captured its effect on nearby parcels. That being said, when we look at velocity vectors along the backward FTLE ridges, we can notice an inflection point in the direction of velocity vectors along the main northern boundary ridge, right around the intersection point (see Fig. 20, left). While looking at velocity vectors along a moving Lagrangian ridge can sometimes be misleading, it is clear here that this point identifies an area of high stretching as seen by the large magnitude velocity vectors on either side of this point farther down the ridge. This point can be found by looking at the zero point of the tangential velocity along a ridge as seen is Fig. 20, right. Note in this figure that the black dots represent the intersection point between the forward and backward ridges. The zero tangential velocity point lags slightly behind due to general westward motion in the flow. This is an example of when using Lagrangian and Eulerian data in conjunction can be beneficial.

4. Discussion

Throughout the lifespan of the dust plume, a dominant ridge of the backward FTLE field acts as a northern boundary for the plume and plays a role in its evolution and eventual splitting. In addition, a vortex structure visible on June 15–16 moves south, intersecting the plume. This structure has a major effect on the plume, drastically changing its shape by flattening and elongating it, propelling the western half towards the Americas at a more rapid rate, and leading to the eventual splitting of the plume. Overall, insight is gained from computing backward time Lagrangian coherent structures, which rely on only current and past velocity data. These structures can be of use in making qualitative, time-sensitive decisions. Had one been able to compute these structures as the event was occurring, one could identify the strong northern ridge and surmise it would act as a barrier, preventing any

dust transport farther north. In addition, the identification of the strong vortex structure on June 15 and the jet-core to its northwest suggests an eventual drastic plume shape change, the speed-up of the western portion, and eventual plume splitting. After the fact, the backward FTLE field assists in understanding the drivers of transport during this massive dust event by identifying the key structures responsible for the fate of the plume.

What additional information do we gain from the utilizing the forward time FTLE structures, which would depend on wind forecasts? Interestingly, the main structures acting as boundaries and those acting as catalysts for deformation are captured within the backward FTLE field itself. The forward FTLE does offer some useful insight however, further demonstrating the strength of the mid June vortex and helping understand why it collided with the plume in the manner it did. The movement of air masses due to the vortical motion can be related to intersection points of attracting and repelling ridges and the resulting "lobe dynamics" (du Toit and Marsden, 2010; Ross and Tallapragada, 2012; Naik et al., 2017).

As demonstrated by the velocity (similarly, streamfunction) and FTLE comparisons, it is clear that the FTLE field, being derived from current *and past* data, can provide more insight into transport events like this one. The velocity fields give simply a snapshot of data with no information about its past evolution. The FTLE ridges identify the material curves within the flow that are most influential on plumes of transported material, its deformation, and fate. As the most significant material lines, in terms of repulsion or attraction of nearby material lines, they have a strong influence on material-laden fluid parcels that come near. This is apparent in mid June as a cascading effect takes place. A strong jet-core propels influential material lines and air mass towards the east, creating a small vortex which leads to a mushrooming effect that eventually collides with the mid June vortex, driving it into the plume and drastically effecting the evolution of the dust storm (see Fig. 16). With this info in real time, a qualitative prediction could have been made about the effect the mid June vortex had on the plume. Using only the velocity fields, no such prediction was evident. For instance, there was not a streamline which acted as a northern plume boundary nor were insights about the fate of the plume captured in the velocity fields.

This is not to say the velocity fields are not useful; they highlight the counter-rotating vortex pattern and made it clear why the plume lingered for as long as it did. In addition, the vorticity field provided insight related to the strength of the counter-rotating vortex pair pattern and the potential alignment of zero vorticity curves with the plume northern boundary attracting ridge.

A number of different approaches could be used to study and perhaps attempt to predict transport in an event like this. Synoptic maps have been used to uncover patterns related to transport. Anomalies relative to the climatology in fields shown in these maps can point to potential exceptional dust events and highlight significant circulation features which play a role in the evolution of the plume (Yu et al., 2021; Francis et al., 2020; Pu and Jin, 2021). These works mainly focus on anomalies in pressure conditions (geopotential heights, NASH) and resulting wind features (strong African easterly jet (AEJ) and anomalous streamfunction patterns). These methods are very useful and highlight

---

[4] In addition to saddle-like points, these points can also behave like homoclinic orbits, homoclinic tangles, and primary intersection points (PIPs). Further investigation is needed to decipher when an intersection point behaves as one of the mentioned candidate points.
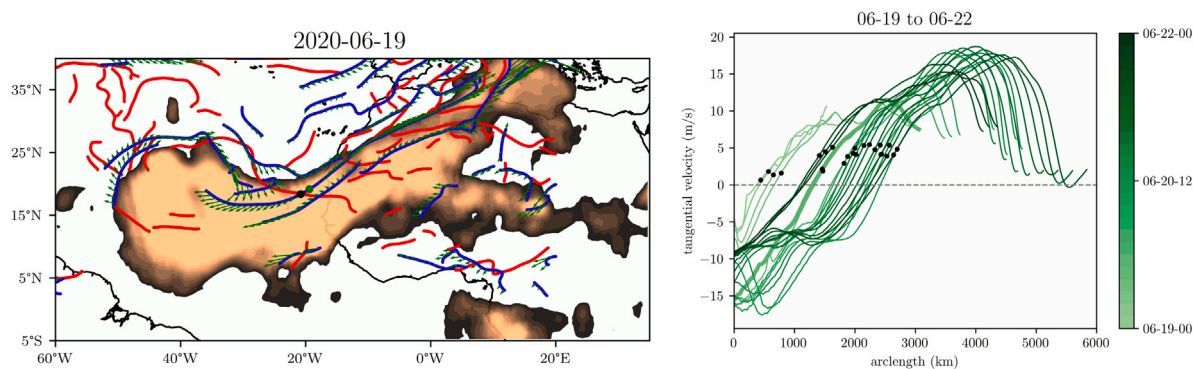
Fig. 20. Left: Backward FTLE ridges (blue) with velocity vectors along ridge (green arrows) overlaid on forward FTLE ridges (red) and OMPS dust data (copper) on June 19, 2020. Black dot represents the intersection point while green dot represents zero tangential velocity point along ridge. Right: Tangential velocity value along portion of main northern ridge of the plume intersecting repelling ridge. The black dots represent the intersection point between the backward and forward ridge which led to the splitting of the plume with the dotted line representing the zero tangential velocity point. Shades of green represent date-time in 3 h increments. Bold line corresponds to same date-time as left figure.

indicators of an extraordinary event while providing a coarser view of the transport. By contrast, FTLE provides finer detail by identifying the structures responsible for transport in a more precise manner. For example, these works point to the anomalous strength and position of the NASH and the associated anticyclonic circulation causing an exceptionally strong AEJ which favored transport to the Americas (Yu et al., 2021). Using FTLE, we identified the strong jet above North America which forced the vortex structure into the plume, causing it to split and propel each portion to the west and east respectively. Indeed, the anticyclonic circulation did strengthen the AEJ but our results suggest that the true culprit to its exceptional strength was the jet we identified that caused the storm to impact the plume. To the authors' knowledge, no work identified this interaction and the significance of these two features beyond noting the role of the anticyclonic circulation in strengthening the AEJ. In addition, we are not aware of any work that uncovered the northern boundary of the plume as the FTLE field did.

For another Lagrangian approach, trajectory models can be used which can calculate particle transport and dispersal in the atmosphere. In most of the literature, tools like these, e.g., the Hybrid Single-Particle Lagrangian Integrated Trajectory (HYSPLIT) model (Stein et al., 2015), are often used to compute backward trajectories and identify possible source regions for these exceptional events (Euphrasie-Clotilde et al., 2021; Liu et al., 2022). In addition, forward trajectory models can be used to verify conclusions drawn from remote-sensing data and modeling (Bi et al., 2024), and to investigate long-term seasonal trends of dust plumes (Mardi et al., 2023). Using trajectory models like this can identify persistent source regions and transport pathways after an event which can be useful information for future events.

The HYSPLIT model has the ability to forecast particle trajectories but the authors are not aware of any work being done utilizing this propagator to forecast long-range dust transport, though it would be interesting to see the accuracy of this tool in a real-time prediction context. Since it would rely on forecast data, it can only be as accurate as the forecast data. One could argue that computing backward FTLE on forecast data would be more advantageous due to the information FTLE provides while relying on less forecast data (FTLE only needs 2D wind velocity while HYSPLIT will need 3D wind velocity and additional meteorological conditions) and being relatively robust to uncertainty in velocity data (Badza et al., 2023). As noted, we are not aware of this being done but would be interested to see the comparison.

Though we do not use FTLE in a true prediction context, applying FTLE in the manner we did (using only current and past data) in real-time could lead to qualitative inferences in a situation like this (e.g., the "northern boundary ridge" would act as a boundary and impede transport to the north, the unfolding of the jet-vortex interaction could imply the splitting of the plume and speed up transport to the Americas, etc.).

Using it in this manner would be quick to implement as well as it would only necessitate the computation of the FTLE field at the current time (given we have computed backward FTLE up to the current time). We do not see how using HYSPLIT on only current and past data could provide similar insight in real-time.

We suggest that the FTLE field (and other coherent structure methods) be integrated as part of the atmospheric scientists toolbox when studying transport events like this and that Eulerian and Lagrangian diagnostics should be used in tandem to get the most out of the information available. This will provide the most complete picture of the transport after the fact and, more importantly, could provide the best information for making predictions in real-time.

5. Conclusion

Using NASA data for velocity fields (MERRA-2) and aerosol index values (OMPS) to represent the "Godzilla" dust plume of 2020, we demonstrated a simple implementation of the FTLE method for transport in geophysical flows. Even with significant simplification, these tools can be employed, essentially in real-time to assist in prediction of the transport of dust or any other contaminant in the atmosphere (e.g., wildfire smoke (Pretorius et al., 2023)). Additionally, these tools can be used after the fact to identify key features responsible for the evolution of this massive dust plume and assist in better understanding the mechanisms by which the transport occurred.

We have shown the advantages of Lagrangian coherent structure (LCS) methods over traditional flow visualization techniques in the atmospheric sciences. By computing quantities which incorporate data outside of the current frame, a more complete picture of transport can be obtained. We do not suggest an abandonment of traditional techniques—far from it. Using Lagrangian tools such as the finite-time Lyapunov exponent (FTLE) field in conjunction with traditional methods and other Eulerian quantities mentioned previously provides the most comprehensive assessment of transport. We suggest researchers use all the tools and techniques available in an optimal manner to get the most out of the available data.

In future work, a more detailed analysis can be performed to obtain a more accurate portrait of the most influential structures of interest. As a caution, the FTLE does not provide information on parabolic and elliptic structures which may be important. Thus, performing parabolic and elliptic LCS computation could yield other important structures that were not captured in the purely hyperbolic investigation. We were able to infer the presence of a jet-core using the attracting structures by its effect on nearby material lines but parabolic LCS would have identified it without the need for inference. In addition, we identified coherent vortices using the LAVD for just a few frames. Employing this tool or other methods to find elliptic LCS for the entire time window

could yield more insight. One could also compute FTLE at a number of different pressure surfaces to see how much the structures differ from the ones we obtain from the averaged velocity field and 600 hPa surface. In addition, these FTLE fields could be "stiched" together to create an approximation of the 3D structures. For a higher fidelity analysis, the FTLE could be computed from the 3D velocity field itself and inertial particle effects of dust could be incorporated. However, comparison with ground truth data would be difficult as the dust data available here via satellite was only a 2D vertical column-averaged data, and only once every 24 h, with little to no vertical resolution. Though not mentioned here, there is a complementary viewpoint which seeks to identify the coherent material sets themselves rather than the material curves that often bound them (Froyland et al., 2010b; Stremler et al., 2011; Grover et al., 2012; Tallapragada and Ross, 2013) which has seen improvements in computationally efficiency in recent years (Froyland and Junge, 2018). A study performing a comparison of these methods in the atmospheric setting would be useful. Like the work done for this dust event, we could perform similar computations for other large scale dust events and see if similar structures persist or different phenomena is observed. Coupling this transport modeling with microbiological analysis could assist in understanding similar past events and mitigating possible negative effects of future ones as well.

We will aim to pursue some of these avenues in future work with most of the focus on computing FTLE over the entire globe for some significant portion of the past to see if we can identify recurrent transport patterns to assist in prediction and obtain a historical record of global atmospheric FTLE. In addition, we have hopes that this data may shed some light on storm formation and intensification. By doing this and other studies, we intend to further demonstrate the usefulness of coherent structure methods to the atmospheric community in hopes of adding to the researchers toolkits when talking problems of this kind.

Ethics

This work does not include studies on human subjects, human data or tissue, or animals

CRediT authorship contribution statement

Albert Jarvis: Writing – review & editing, Writing – original draft, Visualization, Validation, Software, Methodology, Investigation, Formal analysis, Data curation, Conceptualization. **Ali Hossein Mardi:** Writing – review & editing, Writing – original draft, Validation, Software, Resources, Methodology, Investigation, Data curation, Conceptualization. **Hosein Foroutan:** Writing – review & editing, Supervision, Project administration, Methodology, Funding acquisition, Conceptualization. **Shane D. Ross:** Writing – review & editing, Supervision, Resources, Project administration, Methodology, Investigation, Funding acquisition, Formal analysis, Conceptualization.

Declaration of competing interest

The authors declare that they have no known competing financial interests or personal relationships that could have appeared to influence the work reported in this paper.

Data availability

Data will be made available on request. Code used to analyse wind fields, providing diagnostics (FTLE, iLE, and LAVD) and feature extraction (LCS) is available at https://github.com/alb3rtjarvis/numbacs.

Appendix A. Supplementary data

Supplementary material related to this article can be found online at https://doi.org/10.1016/j.atmosenv.2024.120638.

References

Alonso-Pérez, S., Cuevas, E., Querol, X., Guerra, J.C., Pérez, C., 2012. African dust source regions for observed dust outbreaks over the Subtropical Eastern North Atlantic region, above 25 N. J. Arid Environ. 78, 100–109.

Asutosh, A., Vinoj, V., Murukesh, N., Ramisetty, R., Mittal, N., 2022. Investigation of June 2020 giant Saharan dust storm using remote sensing observations and model reanalysis. Sci. Rep. 12 (1), 1–14.

Badza, A., Mattner, T., Balasuriya, S., 2023. How sensitive are Lagrangian coherent structures to uncertainties in data? Physica D 444, 133580.

Bauer, M., Tselioudis, G., Rossow, W.B., 2016. A new climatology for investigating storm influences in and on the extratropics. J. Appl. Meteorol. Climatol. 55 (5), 1287–1303. http://dx.doi.org/10.1175/JAMC-D-15-0245.1, URL: https://journals.ametsoc.org/view/journals/apme/55/5/jamc-d-15-0245.1.xml.

Bi, H., Chen, S., Zhang, D., Wang, Y., Kang, L., Alam, K., Tang, M., Chen, Y., Zhang, Y., Wang, D., 2024. The circumglobal transport of massive african dust and its impacts on the regional circulation in remote atmosphere. Bull. Am. Meteorol. Soc. 105 (3), E605 – E622. http://dx.doi.org/10.1175/BAMS-D-23-0072.1, URL: https://journals.ametsoc.org/view/journals/bams/105/3/BAMS-D-23-0072.1.xml.

Bonasoni, P., Colombo, T., Lenaz, R., Tesi, G., Evangelisti, F., Giovanelli, G., Ravegnani, F., Santaguida, R., 1996. Effect of saharan dust transport on ozone and carbon dioxide concentration. Impact Desert Dust Across Mediterr. 313–322.

Bosilovich, M.G., Lucchesi, R., Suarez, M., 2015. MERRA-2: File Specification Tech. Rep..

Bujack, R., Dutta, S., Rojo, I.B., Zhang, D., Günther, T., 2019. Objective finite-time saddles and their connection to FTLE. In: Eurographics Conference on Visualization. URL: https://api.semanticscholar.org/CorpusID:140081247.

Bujack, R., Middel, A., 2020. State of the art in flow visualization in the environmental sciences. Environ. Earth Sci. 79 (2), 65. http://dx.doi.org/10.1007/s12665-019-8800-4.

Camargo, S.J., Zebiak, S.E., 2002. Improving the detection and tracking of tropical cyclones in atmospheric general circulation models. Weather Forecast. 17 (6), 1152–1162. http://dx.doi.org/10.1175/1520-0434(2002)017<1152:ITDATO>2.0.CO;2, URL: https://journals.ametsoc.org/view/journals/wefo/17/6/1520-0434_2002_017_1152_itdato_2_0_co_2.xml.

Carlson, T.N., Prospero, J.M., 1972. The large-scale movement of saharan air outbreaks over the northern equatorial Atlantic. J. Appl. Meteorol. Climatol. 11 (2), 283–297.

Carvalho, D., 2019. An assessment of NASA's GMAO MERRA-2 reanalysis surface winds. J. Clim. 32 (23), 8261–8281.

Chakraborty, S., Guan, B., Waliser, D.E., da Silva, A.M., Uluatam, S., Hess, P., 2021. Extending the atmospheric river concept to aerosols: Climate and air quality impacts. Geophys. Res. Lett. 48 (9), e2020GL091827. http://dx.doi.org/10.1029/2020GL091827, e2020GL091827 2020GL091827. URL: https://agupubs.onlinelibrary.wiley.com/doi/abs/10.1029/2020GL091827, arXiv:https://agupubs.onlinelibrary.wiley.com/doi/pdf/10.1029/2020GL091827.

Chang, E.K.M., 2017. Projected significant increase in the number of extreme extratropical cyclones in the southern hemisphere. J. Clim. 30 (13), 4915–4935. http://dx.doi.org/10.1175/JCLI-D-16-0553.1, URL: https://journals.ametsoc.org/view/journals/clim/30/13/jcli-d-16-0553.1.xml.

Chiapello, I., Bergametti, G., Chatenet, B., Bousquet, P., Dulac, F., Soares, E.S., 1997. Origins of African dust transported over the northeastern tropical Atlantic. J. Geophys. Res.: Atmos. 102 (D12), 13701–13709.

Coulliette, C., Wiggins, S., 2001. Intergyre transport in a wind-driven, quasigeostrophic double gyre: an application of lobe dynamics. Nonlinear Process. Geophys. 8, 69–94.

Curbelo, J., Rypina, I.I., 2023. A three dimensional Lagrangian analysis of the smoke plume from the 2019/2020 Australian wildfire event. J. Geophys. Res.: Atmos. 128 (21), e2023JD039773. http://dx.doi.org/10.1029/2023JD039773, e2023JD039773 2023JD039773. URL: https://agupubs.onlinelibrary.wiley.com/doi/abs/10.1029/2023JD039773, arXiv:https://agupubs.onlinelibrary.wiley.com/doi/pdf/10.1029/2023JD039773.

Dawson, A., 2016. Windspharm: A high-level library for global wind field computations using spherical harmonics. J. Open Res. Softw. http://dx.doi.org/10.5334/jors.129.

Dellnitz, M., Froyland, G., Horenkamp, C., Padberg-Gehle, K., Gupta, A.S., 2009. Seasonal variability of the subpolar gyres in the Southern Ocean: a numerical investigation based on transfer operators. Nonlinear Process. Geophys. 16, 655–664.

Euphrasie-Clotilde, L., Plocoste, T., Brute, F.-N., 2021. Particle size analysis of african dust haze over the last 20 years: A focus on the extreme event of June 2020. Atmosphere 12 (4), 502.

Francis, D., Fonseca, R., Nelli, N., Cuesta, J., Weston, M., Evan, A., Temimi, M., 2020. The atmospheric drivers of the major saharan dust storm in June 2020. Geophys. Res. Lett. 47 (24), http://dx.doi.org/10.1029/2020GL090102.

Froyland, G., Junge, O., 2018. Robust FEM-based extraction of finite-time coherent sets using scattered, sparse, and incomplete trajectories. SIAM J. Appl. Dyn. Syst. 17 (2), 1891–1924. http://dx.doi.org/10.1137/17M1129738.

Froyland, G., Padberg, K., England, M.H., Treguier, A.M., 2007. Detection of coherent oceanic structures via transfer operators. Phys. Rev. Lett. 98, 224503.

Froyland, G., Santitissadeekorn, N., Monahan, A., 2010a. Optimally coherent sets in geophysical flows: A new approach to delimiting the stratospheric polar vortex. Phys. Rev. E 82, 056311.

Froyland, G., Santitissadeekorn, N., Monahan, A., 2010b. Transport in time-dependent dynamical systems: Finite-time coherent sets. Chaos 20 (4), 043116. http://dx.doi.org/10.1063/1.3502450, arXiv:https://pubs.aip.org/aip/cha/article-pdf/doi/10.1063/1.3502450/13278544/043116_1_online.pdf.

Garaboa-Paz, D., Eiras-Barca, J., Huhn, F., Pérez-Muũuzuri, V., 2015. Lagrangian coherent structures along atmospheric rivers. Chaos 25 (6), 063105. http://dx.doi.org/10.1063/1.4919768.

Gelaro, R., McCarty, W., Suarez, M.J., Todling, R., Molod, A., Takacs, L., Randles, C.A., Darmenov, A., Bosilovich, M.G., Reichle, R., Wargan, K., Coy, L., Cullather, R., Draper, C., Akella, S., Buchard, V., Conaty, A., da Silva, A.M., Gu, W., Kim, G.-K., Koster, R., Lucchesi, R., Merkova, D., Nielsen, J.E., Partyka, G., Pawson, S., Putman, W., Rienecker, M., Schubert, S.D., Sienkiewicz, M., Zhao, B., 2017. The modern-era retrospective analysis for research and applications, version 2 (MERRA-2). J. Clim. 30 (14), 5419–5454. http://dx.doi.org/10.1175/JCLI-D-16-0758.1, URL: https://journals.ametsoc.org/view/journals/clim/30/14/jcli-d-16-0758.1.xml.

Gläser, G., Wernli, H., Kerkweg, A., Teubler, F., 2015. The transatlantic dust transport from North Africa to the Americas—Its characteristics and source regions. J. Geophys. Res.: Atmos. 120 (21), 11–231.

Global Modeling and Assimilation Office (GMAO), 2015. MERRA-2 inst3_3d_asm_Np: 3d, 3-Hourly, Instantaneous, Pressure-Level, Assimilation, Assimilated Meteorological Fields V5.12.4. Goddard Earth Sciences Data and Information Services Center (GES DISC), Greenbelt, MD, USA, http://dx.doi.org/10.5067/QBZ6MG944HW0, (Accessed 22 September 2023).

Grover, P., Ross, S.D., Stremler, M.A., Kumar, P., 2012. Topological chaos, braiding and bifurcation of almost-cyclic sets. Chaos 22 (4), 043135.

Günther, M., Horváth, Á., Bresky, W., Daniels, J., Buehler, S.A., 2021. Lagrangian coherent structures and vortex formation in high spatiotemporal-resolution satellite winds of an atmospheric Kármán vortex street. J. Geophys. Res.: Atmos. 126 (19), e2021JD035000. http://dx.doi.org/10.1029/2021JD035000, URL: https://agupubs.onlinelibrary.wiley.com/doi/abs/10.1029/2021JD035000.

Haller, G., 2011. A variational theory of hyperbolic Lagrangian coherent structures. Phys. D 240, 574–598.

Haller, G., 2015. Lagrangian coherent structures. Annu. Rev. Fluid Mech. 47 (1), 137–162. http://dx.doi.org/10.1146/annurev-fluid-010313-141322.

Haller, G., 2023. Transport Barriers and Coherent Structures in Flow Data: Advective, Diffusive, Stochastic and Active Methods. Cambridge University Press.

Haller, G., Hadjighasem, A., Farazmand, M., Huhn, F., 2016. Defining coherent vortices objectively from the vorticity. J. Fluid Mech. 795, 136–173. http://dx.doi.org/10.1017/jfm.2016.151.

Haller, G., Karrasch, D., Kogelbauer, F., 2018. Material barriers to diffusive and stochastic transport. Proc. Natl. Acad. Sci. 115 (37), 9074–9079. http://dx.doi.org/10.1073/pnas.1720177115, URL: https://www.pnas.org/doi/abs/10.1073/pnas.1720177115.

Haller, G., Yuan, G., 2000. Lagrangian coherent structures and mixing in two-dimensional turbulence. Phys. D 147, 352–370.

Hersbach, H., Bell, B., Berrisford, P., Biavati, G., Horányi, A., Muñoz Sabater, J., Nicolas, J., Peubey, C., Radu, R., Rozum, I., Schepers, A., Soci, C., Dee, D., Thépaut, J.-N., 2023a. ERA5 hourly data on pressure levels from 1940 to present. Copernicus Climate Change Service (C3S) Climate Data Store (CDS). http://dx.doi.org/10.24381/cds.bd0915c6, (Accessed 13 April 2024).

Hersbach, H., Bell, B., Berrisford, P., Biavati, G., Horányi, A., Muñoz Sabater, J., Nicolas, J., Peubey, C., Radu, R., Rozum, I., Schepers, A., Soci, C., Dee, D., Thépaut, J.-N., 2023b. ERA5 hourly data on single levels from 1940 to present. Copernicus climate change service (C3S) climate data store (CDS). http://dx.doi.org/10.24381/cds.adbb2d47, (Accessed 13 April 2024).

Joseph, B., Legras, B., 2002. Relation between kinematic boundaries, stirring, and barriers for the antarctic polar vortex. J. Atmos. Sci. 59, 1198–1212.

Karyampudi, V.M., Palm, S.P., Reagen, J.A., Fang, H., Grant, W.B., Hoff, R.M., Moulin, C., Pierce, H.F., Torres, O., Browell, E.V., et al., 1999. Validation of the Saharan dust plume conceptual model using lidar, Meteosat, and ECMWF data. Bull. Am. Meteorol. Soc. 80 (6), 1045–1076.

Khatibi, A., Krauter, S., 2021. Validation and performance of satellite meteorological dataset MERRA-2 for solar and wind applications. Energies 14 (4), 882.

Lekien, F., Ross, S.D., 2010. The computation of finite-time Lyapunov exponents on unstructured meshes and for non-Euclidean manifolds. Chaos 20, 017505.

Liu, Q., Huang, Z., Hu, Z., Dong, Q., Li, S., 2022. Long-range transport and evolution of saharan dust over east Asia from 2007 to 2020. J. Geophys. Res.: Atmos. 127 (18), e2022JD036974. http://dx.doi.org/10.1029/2022JD036974, e2022JD036974 2022JD036974. URL: https://agupubs.onlinelibrary.wiley.com/doi/abs/10.1029/2022JD036974.

Liu, Y., Wilson, C., Green, M.A., Hughes, C.W., 2018. Gulf stream transport and mixing processes via coherent structure dynamics. J. Geophys. Res.: Oceans 123 (4), 3014–3037. http://dx.doi.org/10.1002/2017JC013390, URL: https://agupubs.onlinelibrary.wiley.com/doi/abs/10.1002/2017JC013390, arXiv:https://agupubs.onlinelibrary.wiley.com/doi/pdf/10.1002/2017JC013390.

Lopesino, C., Balibrea-Iniesta, F., García-Garrido, V.J., Wiggins, S., Mancho, A.M., 2017. A theoretical framework for Lagrangian descriptors. Int. J. Bifurcation Chaos 27 (01), 1730001.

MacKay, R.S., Meiss, J.D., Percival, I.C., 1984. Transport in Hamiltonian systems. Phys. D 13, 55–81.

Mancho, A.M., Small, D., Wiggins, S., 2006. A tutorial on dynamical systems concepts applied to Lagrangian transport in oceanic flows defined as finite time data sets: Theoretical and computational issues. Phys. Rep. 437 (3), 55–124. http://dx.doi.org/10.1016/j.physrep.2006.09.005, URL: http://www.sciencedirect.com/science/article/pii/S0370157306003401.

Mardi, A.H., HILARIO, M.R., Hanlon, R., González-Martín, C., Schmale, D., Sorooshian, A., Foroutan, H., 2023. Long-Term Seasonal Trends in Sources and Pathways of Trans-Atlantic Dust Plumes and their Implications for Transport of Microorganisms. Authorea, Inc., http://dx.doi.org/10.22541/essoar.167979593.35998646/v1.

Meiss, J.D., 1992. Symplectic maps, variational principles, and transport. Rev. Mod. Phys. 64, 795–848.

Naik, S., Lekien, F., Ross, S.D., 2017. Computational method for phase space transport with applications to lobe dynamics and rate of escape. Regul. Chaotic Dyn. 22 (3), 272–297. http://dx.doi.org/10.1134/S1560354717030078.

Newton, P.K., 2001. The N-vortex problem: Analytical techniques. In: Appl. Math. Sci. Series, vol. 145, Springer-Verlag, Berlin-Heidelberg-New York.

Nolan, P.J., Foroutan, H., Ross, S.D., 2020a. Pollution transport patterns obtained through generalized Lagrangian coherent structures. Atmosphere 11 (2), http://dx.doi.org/10.3390/atmos11020168.

Nolan, P., Serra, M., Ross, S., 2020b. Finite-time Lyapunov exponents in the instantaneous limit and material transport. Nonlinear Dynam. 100, 3825–3852.

Peacock, T., Haller, G., 2013. Lagrangian coherent structures: The hidden skeleton of fluid flows. Phys. Today 66 (2), 41.

Peng, J., Peterson, R., 2012. Attracting structures in volcanic ash transport. Atmos. Environ. 48, 230–239.

Pretorius, I., Schou, W.C., Richardson, B., Ross, S.D., Withers, T.M., Schmale, III, D.G., Strand, T.M., 2023. In the wind: Invasive species travel along predictable atmospheric pathways. Ecol. Appl. 33 (3), e2806. http://dx.doi.org/10.1002/eap.2806, URL: https://esajournals.onlinelibrary.wiley.com/doi/abs/10.1002/eap.2806, arXiv:https://esajournals.onlinelibrary.wiley.com/doi/pdf/10.1002/eap.2806.

Pu, B., Jin, Q., 2021. A record-breaking trans-atlantic african dust plume associated with atmospheric circulation extremes in june 2020. Bull. Am. Meteorol. Soc. 102 (7), E1340 – E1356. http://dx.doi.org/10.1175/BAMS-D-21-0014.1, URL: https://journals.ametsoc.org/view/journals/bams/102/7/BAMS-D-21-0014.1.xml.

Remini, B., 2020. Awesome, the dust of the Sahara in the sky of the America continent Godzilla, the biggest dust storm in half a century. LARHYSS Journal (43), 139–167, P-ISSN 1112-3680/E-ISSN 2521-9782.

Ross, S.D., Tallapragada, P., 2012. Detecting and exploiting chaotic transport in mechanical systems. In: Banerjee, S., Rondoni, L., Mitra, M. (Eds.), In: Applications of Chaos and Nonlinear Dynamics in Science and Engineering, vol. 2, Springer, New York, pp. 155–183.

Rutherford, B., Dangelmayr, G., Montgomery, M.T., 2012. Lagrangian coherent structures in tropical cyclone intensification. Atmos. Chem. Phys. 12 (12), 5483–5507. http://dx.doi.org/10.5194/acp-12-5483-2012, URL: https://acp.copernicus.org/articles/12/5483/2012/.

Sadlo, F., Weiskopf, D., 2010. Time-dependent 2-D vector field topology: An approach inspired by Lagrangian coherent structures. Comput. Graph. Forum 29, URL: https://api.semanticscholar.org/CorpusID:428227.

Santitissadeekorn, N., Froyland, G., Monahan, A., 2010. Optimally coherent sets in geophysical flows: a transfer-operator approach to delimiting the stratospheric polar vortex. Phys. Rev. E (3) 82 (5 Pt 2), 056311 – ?.

Sapsis, T., Haller, G., 2009. Inertial particle dynamics in a hurricane. J. Atmos. Sci. 66 (8), 2481–2492. http://dx.doi.org/10.1175/2009JAS2865.1, URL: https://journals.ametsoc.org/view/journals/atsc/66/8/2009jas2865.1.xml.

Schmale, D.G., Ross, S.D., 2015. Highways in the sky: Scales of atmospheric transport of plant pathogens. Annu. Rev. Phytopathol. 53 (1), 591–611.

Schmale, D.G., Ross, S.D., 2017. High-flying microbes: Aerial drones and chaos theory help researchers explore the many ways that microorganisms spread havoc around the world. Sci. Am. February, 32–37.

Schmale, III, D., Ross, S., Fetters, T., Tallapragada, P., Wood-Jones, A., Dingus, B., 2012. Isolates of Fusarium graminearum collected 40–320 meters above ground level cause Fusarium head blight in wheat and produce trichothecene mycotoxins. Aerobiologia 28 (1), 1–11.

Senatore, C., Ross, S.D., 2011. Detection and characterization of transport barriers in complex flows via ridge extraction of the finite time Lyapunov exponent field. Internat. J. Numer. Methods Engrg. 86, 1163–1174. http://dx.doi.org/10.1002/nme.3101.

Serra, M., Sathe, P., Beron-Vera, F., Haller, G., 2017. Uncovering the edge of the polar vortex. J. Atmos. Sci. 74 (11), 3871–3885. http://dx.doi.org/10.1175/JAS-D-17-0052.1, URL: https://journals.ametsoc.org/view/journals/atsc/74/11/jas-d-17-0052.1.xml.

Serra, M., Sathe, P., Rypina, I., Kirincich, A., Ross, S.D., Lermusiaux, P., Allen, A., Peacock, T., Haller, G., 2020. Search and rescue at sea aided by hidden flow structures. Nature Commun. 11 (1), 2525.

Shadden, S.C., Dabiri, J.O., Marsden, J.E., 2006. Lagrangian analysis of fluid transport in empirical vortex ring flows. Phys. Fluids 18 (4), 047105. http://dx.doi.org/10.1063/1.2189885.

Shadden, S.C., Lekien, F., Marsden, J.E., 2005. Definition and properties of Lagrangian coherent structures: mixing and transport in two-dimensional aperiodic flows. Phys. D 212, 271–304.

Steger, C., 1998. An unbiased detector of curvilinear structures. IEEE Trans. Pattern Anal. Mach. Intell. 20 (2), 113–125. http://dx.doi.org/10.1109/34.659930.

Stein, A.F., Draxler, R.R., Rolph, G.D., Stunder, B.J.B., Cohen, M.D., Ngan, F., 2015. NOAA's HYSPLIT atmospheric transport and dispersion modeling system. Bull. Am. Meteorol. Soc. 96 (12), 2059–2077. http://dx.doi.org/10.1175/BAMS-D-14-00110.1, URL: https://journals.ametsoc.org/view/journals/bams/96/12/bams-d-14-00110.1.xml.

Stremler, M.A., Ross, S.D., Grover, P., Kumar, P., 2011. Topological chaos and periodic braiding of almost-cyclic sets. Phys. Rev. Lett. 106, 114101.

Strogatz, S.H., 2014. Nonlinear Dynamics and Chaos: With Applications to Physics, Biology, Chemistry, and Engineering, second ed. CRC Press.

Sudharsan, M.B., Brunton, S.L., Riley, J.J., 2015. Lagrangian coherent structures and inertial particle dynamics. Phys. Rev. E 93 3, 033108, URL: https://api.semanticscholar.org/CorpusID:32179502.

Tallapragada, P., Ross, S.D., 2008. Particle segregation by Stokes number for small neutrally buoyant spheres in a fluid. Phys. Rev. E 78, 036308.

Tallapragada, P., Ross, S.D., 2013. A set oriented definition of finite-time Lyapunov exponents and coherent sets. Commun. Nonlinear Sci. Numer. Simul. 18 (5), 1106–1126.

Tallapragada, P., Ross, S.D., Schmale, D., 2011. Lagrangian coherent structures are associated with fluctuations in airborne microbial populations. Chaos 21, 033122.

du Toit, P.C., Marsden, J.E., 2010. Horseshoes in hurricanes. J. Fixed Point Theory Appl. 7 (2), 351–384. http://dx.doi.org/10.1007/s11784-010-0028-6.

Torres, O., 2019. OMPS-NPP L2 NM Aerosol Index Swath Orbital V2, vol. 10, Goddard Earth Sciences Data and Information Services Center (GES DISC), Greenbelt, MD, USA, p. 89.

Walker, E., Mitchell, D., Seviour, W., 2020. The numerous approaches to tracking extratropical cyclones and the challenges they present. Weather 75 (11), 336–341. http://dx.doi.org/10.1002/wea.3861, URL: https://rmets.onlinelibrary.wiley.com/doi/abs/10.1002/wea.3861, arXiv:https://rmets.onlinelibrary.wiley.com/doi/pdf/10.1002/wea.3861.

Wiggins, S., 2003. Introduction to applied nonlinear dynamical systems and chaos, second ed. Texts in Applied Mathematics Science, vol. 2, Springer-Verlag, Berlin.

Yang, K., Dickerson, R.R., Carn, S.A., Ge, C., Wang, J., 2013. First observations of SO2 from the satellite suomi NPP OMPS: Widespread air pollution events over China. Geophys. Res. Lett. 40 (18), 4957–4962.

Yu, H., Chin, M., Bian, H., Yuan, T., Prospero, J.M., Omar, A.H., Remer, L.A., Winker, D.M., Yang, Y., Zhang, Y., Zhang, Z., 2015. Quantification of trans-Atlantic dust transport from seven-year (2007–2013) record of CALIPSO lidar measurements. Remote Sens. Environ. 159, 232–249. http://dx.doi.org/10.1016/j.rse.2014.12.010, URL: https://www.sciencedirect.com/science/article/pii/S0034425714005021.

Yu, H., Remer, L.A., Kahn, R.A., Chin, M., Zhang, Y., 2013. Satellite perspective of aerosol intercontinental transport: From qualitative tracking to quantitative characterization. Atmos. Res. 124, 73–100. http://dx.doi.org/10.1016/j.atmosres.2012.12.013, URL: https://www.sciencedirect.com/science/article/pii/S0169809513000070.

Yu, H., Tan, Q., Zhou, L., Zhou, Y., Bian, H., Chin, M., Ryder, C.L., Levy, R.C., Pradhan, Y., Shi, Y., et al., 2021. Observation and modeling of the historic "Godzilla" African dust intrusion into the Caribbean Basin and the southern US in June 2020. Atmos. Chem. Phys. 21 (16), 12359–12383.